

Exotica in the Globular Cluster M4, Studied with Chandra, HST, and the VLA

Phyllis M. Lugger,¹★ Haldan N. Cohn,¹ Craig O. Heinke,² Jiaqi Zhao,² Yue Zhao,³ and Jay Anderson⁴

¹Department of Astronomy, Indiana University, 727 E. Third St., Bloomington, IN 47405, USA

²Department of Physics, University of Alberta, Edmonton, AB T6G 2G7, Canada

³Department of Physics and Astronomy, University of Southampton, University Road, Southampton SO17 1BJ, UK

⁴Space Telescope Science Institute, 3700 San Martin Dr., Baltimore, MD 21218, USA

Accepted 2023 June 13. Received 2023 Jun 11; in original form 2023 February 14

ABSTRACT

Using the Hubble Ultraviolet Globular Cluster Survey (HUGS) and additional *HST* archival data, we have carried out a search for optical counterparts to the low-luminosity *Chandra* X-ray sources in the globular cluster M4 (NGC 6121). We have also searched for optical or X-ray counterparts to radio sources detected by the VLA. We find 24 new confident optical counterparts to *Chandra* sources for a total of 40, including the 16 previously identified. Of the 24 new identifications, 18 are stellar coronal X-ray sources (active binaries, ABs), the majority located along the binary sequence in a $V_{606} - I_{814}$ colour-magnitude diagram and generally showing an $H\alpha$ excess. In addition to confirming the previously detected cataclysmic variable (CV, CX4), we identify one confident new CV (CX76), and two candidates (CX81 and CX101). One MSP is known in M4 (CX12), and another strong candidate has been suggested (CX1); we identify some possible MSP candidates among optical and radio sources, such as VLA20, which appears to have a white dwarf counterpart. One X-ray source with a sub-subgiant optical counterpart and a flat radio spectrum (CX8, VLA31) is particularly mysterious. The radial distribution of X-ray sources suggests a relaxed population of average mass $\sim 1.2 - 1.5 M_{\odot}$. Comparing the numbers of ABs, MSPs, and CVs in M4 with other clusters indicates that AB numbers are proportional to cluster mass (primordial population), MSPs to stellar encounter rate (dynamically formed population), while CVs seem to be produced both primordially and dynamically.

Key words: globular clusters: individual: NGC 6121 – binaries: close – X-rays: binaries – novae, cataclysmic variables – stars: activity – Hertzsprung–Russell and colour-magnitude diagrams

1 INTRODUCTION

The nearest globular cluster, M4 (NGC 6121), has long been known to host a substantial population of low-luminosity X-ray sources ($L_X \lesssim 10^{34}$ erg s⁻¹; Bassa et al. 2004; Verbunt 2001). M4 has a moderate central density, thus providing an important basis of comparison with the well-studied nearby clusters ω Cen (Cool et al. 2013; Henleywillis et al. 2018), which has a low central density, 47 Tuc (Heinke et al. 2005; Rivera Sandoval et al. 2018), which has a moderate central density, and NGC 6397 (Cohn et al. 2010) and NGC 6752 (Lugger et al. 2017; Cohn et al. 2021), which

are core collapsed and thus have extremely high central densities. The Bahramian et al. (2020) catalogue of *Chandra* sources in 38 globular clusters, which is based on deep ACIS (Advanced CCD Imaging Spectrometer) imaging, lists 161 sources in the entire ACIS field of M4. Of these, 52 sources are within the central 1.7 arcmin radius region, which corresponds to the half-width of the *HST* ACS/WFC¹ field of view. The class of low-luminosity X-ray sources includes cataclysmic variables (CVs), magnetically active binaries (ABs), millisecond pulsars (MSPs), and (potentially) black hole (BH) and/or neutron star X-ray binaries (van den Berg 2020).

In order to build on previous efforts to identify and charac-

★ E-mail: lugger@iu.edu (PML)

¹ Advanced Camera for Surveys/Wide Field Channel

Table 1. Comparison of the properties of M4 with a sample of nearby, well-studied clusters. Values for solar distance (d_{\odot}), central density (ρ_0), and mass (M) are from [Baumgardt et al. \(2021\)](#), interaction rates (Γ) are from [Bahramian et al. \(2013\)](#), X-ray emissivities ($\xi_X = L_X/M$) are from [Heinke et al. \(2020\)](#). Limiting L_X values are from [Bahramian et al. \(2020\)](#) for M4 and NGC 6397, from [Heinke et al. \(2005\)](#) for 47 Tuc, from [Cool et al. \(2013\)](#) for ω Cen, and from [Cohn et al. \(2021\)](#) for NGC 6752. The value for ω Cen applies to the centre of this large cluster; the sensitivity falls off with radial offset.

Cluster	d_{\odot} [kpc]	$\log \rho_0$ [$M_{\odot} \text{pc}^{-3}$]	$\log M$ [M_{\odot}]	Γ	ξ_X [$10^{27} \text{erg s}^{-1} M_{\odot}^{-1}$]	Exposure [ks]	$\log L_{X,\text{lim}}$ [erg s^{-1}]
47 Tuc	4.5	4.4	6.0	1000	5.8	540	29.9
ω Cen	5.4	3.3	6.6	90	0.9	291	30.1
M4	1.9	4.2	4.9	27	3.6	119	29.5
NGC 6397	2.5	6.4	5.0	84	15.0	325	29.0
NGC 6752	4.1	5.9	5.4	401	4.4	346	29.5

terise the X-ray source population of M4, we employed photometry from the Hubble Ultraviolet Globular Cluster Survey (HUGS, [Piotto et al. 2015](#); [Nardiello et al. 2018](#)) and additional archival *HST* data. The [Bahramian et al. \(2020\)](#) *Chandra* source catalogue and the HUGS photometry database both supersede those used in the previous comprehensive study of *Chandra* sources and their optical counterparts in M4 by [Bassa et al. \(2004, 2005\)](#).

1.1 Background

Hard binaries play a critical role in cluster dynamical evolution, since they initially support cluster cores against collapse ([Kremer et al. 2020](#)) and later halt deep collapse, leading to core bounce and subsequent oscillations ([Hut et al. 1992](#); [Vesperini 2010](#)). The central question addressed by this study is how compact binary X-ray source populations are shaped by primordial formation and dynamical evolutionary processes. This issue has been the subject of considerable research, as recently reviewed by [Cheng et al. \(2018\)](#), [Belloni et al. \(2019\)](#), and [Heinke et al. \(2020\)](#). Globular clusters have long been known to be ~ 100 times overabundant in low-mass X-ray binaries (LMXBs, with $L_X \gtrsim 10^{35} \text{erg s}^{-1}$) relative to the field, pointing to a dynamical origin of these neutron-star-containing binaries in dense clusters ([Clark 1975](#)). Subsequent studies showed that the total number of X-ray sources in a globular cluster scales with the density-dependent interaction rate $\Gamma \propto \int_V (\rho^2/v) dV \propto \rho_0^2 r_c^3/v_0$, where ρ_0 is central density, r_c is the core radius, and v_0 is the central velocity dispersion (the second expression approximates the interactions as all occurring in a constant-density cluster core; [Johnston & Verbunt 1996](#); [Heinke et al. 2003](#); [Pooley et al. 2003](#); [Pooley & Hut 2006](#); [Bahramian et al. 2013](#)). However, it has been observed that the low-density populations of open clusters have X-ray emissivities (X-ray luminosity per unit mass) that are higher than those of all but the highest density globular clusters ([Verbunt 2000](#); [Ge et al. 2015](#); [van den Berg 2020](#)). For the open clusters NGC 6791 and M67, the number of CVs per unit mass is higher than in the field, which is consistent with the emissivity result. The origin of this is not certain, but the high evaporative mass loss of open clusters, combined with mass segregation, is a plausible explanation – the remaining mass in the clusters is concentrated toward high-mass objects, especially binaries ([Verbunt 2000](#)). It appears that a complex interaction between binary formation and destruction determines the relative numbers of CVs and ABs in a globular cluster, and the luminosity functions of each of these groups ([Ivanova et al. 2006](#); [Belloni et al. 2019](#); [Heinke et al. 2020](#)).

Previous *Chandra* and *HST* studies of the X-ray emitting binary populations in other nearby globular clusters include those of NGC 6397 ([Grindlay et al. 2001b](#); [Taylor et al. 2001](#); [Bogdanov et al. 2010](#); [Cohn et al. 2010](#)), NGC 6752 ([Pooley et al. 2002](#);

[Thomson et al. 2012](#); [Lugger et al. 2017](#); [Cohn et al. 2021](#)), 47 Tuc ([Grindlay et al. 2001a](#); [Edmonds et al. 2003b,a](#); [Heinke et al. 2005](#); [Bhattacharya et al. 2017](#); [Cheng et al. 2018](#); [Rivera Sandoval et al. 2018](#)), and ω Cen ([Haggard et al. 2009](#); [Cool et al. 2013](#); [Henley-willis et al. 2018](#)). A compilation of the properties of these clusters and a summary of the *Chandra* observations are given in Table 1.

1.2 CVs in Globular Clusters

Cataclysmic variables are semi-detached binary systems in which a white dwarf primary accretes material from a main-sequence secondary that overflows its Roche lobe. The term ‘cataclysmic’ refers to the very large amplitude luminosity variations that may be observed in these systems. CVs are the most numerous type of accreting X-ray source, and have been clearly identified in a number of globular clusters (e.g. [Cool et al. 1995](#); [Pooley et al. 2002](#); [Edmonds et al. 2003b](#); [Knigge et al. 2003](#); [Cohn et al. 2010](#); [Thomson et al. 2012](#); [Cool et al. 2013](#); [Lugger et al. 2017](#); [Rivera Sandoval et al. 2018](#); [Cohn et al. 2021](#)). Identification of an X-ray source’s optical counterpart as a likely CV generally has been claimed using one or more of: blue colours, photometric $H\alpha$ excess, optical variability, or a CV-type emission-line spectrum ([Knigge 2012](#)), along with a proper motion consistent with the cluster. A majority of the strong candidate CVs in clusters have been identified using the trio of *Chandra* X-ray emission, blue colours, and $H\alpha$ excess. LMXBs, and MSPs with nondegenerate companions (redbacks), can appear similar to CVs, but both classes are significantly rarer than CVs (e.g. in 47 Tuc, there are 43 CVs, 6 quiescent LMXBs, and 3 redbacks; [Rivera Sandoval et al. 2018](#); [Heinke et al. 2005](#); [Miller-Jones et al. 2015](#); [Ridolfi et al. 2021](#)).

The production of CVs in globular clusters is complex, as some CVs are produced through dynamical channels, such as exchange interactions with primordial binaries, and possibly tidal captures, while others are of primordial origin (e.g. [Davies 1997](#); [Ivanova et al. 2006](#); [Shara & Hurley 2006](#); [Belloni et al. 2019](#)). Dynamical production of CVs in dense clusters is supported by the correlation between the stellar encounter rates Γ and numbers of cluster sources ([Pooley & Hut 2006](#); [Heinke et al. 2006](#); [Bahramian et al. 2013](#)). For a sufficiently large CV population in a cluster, the spatial distribution and luminosity function of the CVs provide information on their ages and dynamical state.

Theoretically, lower-density clusters are expected to have more primordially-formed CVs than dynamically-formed CVs ([Davies 1997](#); [Belloni et al. 2019](#)), and there is observational support for this prediction ([Kong et al. 2006](#); [Haggard et al. 2009](#); [Cheng et al. 2018](#); [Belloni et al. 2019](#)). It has also been suggested that many primordial soft binaries in clusters have been destroyed by dynamical interactions, thus preventing them from becoming X-ray-emitting

Table 2. CV numbers in M4 and a sample of nearby, well-studied clusters. ‘Candidate’ includes ‘Confirmed,’ where confirmation is usually by a detection of excess H α emission.

Cluster	N_{CV}			Refs
	Predicted	Candidate	Confirmed	
47 Tuc	36	44	29	1,2
ω Cen	144	27	6	3,4
M4	4	4	1	5,6
NGC 6397	4	15	11	7
NGC 6752	11	18	7	8,9,10

Notes: 1: Edmonds et al. (2003b), 2: Rivera Sandoval et al. (2018), 3: Cool et al. (2013), 4: Henleywillis et al. (2018), 5: Bassa et al. (2004, 2005), 6: this work, 7: Cohn et al. (2010), 8: Pooley et al. (2003), 9: Lugger et al. (2017), 10: Cohn et al. (2021)

close binaries (Ivanova et al. 2005; Fregeau et al. 2009; Belloni et al. 2019). In high-density clusters, formation of new CVs by dynamical processes may dominate over primordial CV destruction, leading to an excess number of CVs relative to the observed X-ray emissivity of the field CV population.

Two recent studies have investigated the dependence of X-ray emissivity on cluster properties such as central density, mass, and interaction rate (Cheng et al. 2018; Heinke et al. 2020). The latter study found that for globular clusters with central densities above $10^4 M_{\odot} \text{pc}^{-3}$, X-ray emissivity and central density correlate. This supports the prediction that dynamical formation of CVs is dominant over primordial formation in these denser clusters.

Table 2 provides a comparison of the number of CV candidates in a cluster to the number predicted for its mass (Table 1), based on the number of CVs per unit stellar mass in the solar vicinity. The identification of CVs depends on both X-ray and optical sensitivity in a complex way (a full analysis is outside the scope of this paper), so the numbers of confirmed CVs should be taken as a lower limit on the true CV numbers. The local density of CVs with $L_X \geq 10^{30} \text{erg s}^{-1}$ is $\sim 2 \times 10^{-6} \text{pc}^{-3}$ (Pretorius & Knigge 2012). Taken with the local mass density of $0.05 M_{\odot} \text{pc}^{-3}$ (Chabrier 2001), this gives a field CV number per unit mass of $\sim 4 \times 10^{-5} M_{\odot}^{-1}$. Table 2 shows there is an excess of CV candidates in the high-density globular clusters NGC 6397 and NGC 6752, relative to the number predicted from the field density (or observed in the moderate-density cluster M4), especially for NGC 6397. This may be a result of dynamical interactions in the collapsed cores. As M4 is nearby, with (now) rather deep X-ray and moderately deep optical observations, we plan to use it as a baseline for future comparisons among clusters.

Bright CVs should be younger on average, as CVs often start with (relatively) massive companions, and the companion’s optical luminosity and mass loss rate both decay with time due to mass loss to the white dwarf (Hellier 2001). Studies of NGC 6397 (Cohn et al. 2010), NGC 6752 (Lugger et al. 2017; Cohn et al. 2021), 47 Tuc (Rivera Sandoval et al. 2018), and ω Cen (Cool et al. 2013) have revealed significant populations of X-ray and optically faint CVs, which are expected to have orbital periods generally below 2 hours, based on predictions from binary evolution (Ivanova et al. 2006; Belloni et al. 2019). These simulations predict two (or more) times as many detectable CVs below the 2–3 h period gap as above it.

Observations of local CVs by Pala et al. (2020) find 3–8 times more CVs below the period gap, and suggest that $M_R \approx 9$ roughly divides CVs at the period gap. In 47 Tuc, there are about 3 \times more CVs below the period gap than above it (Rivera Sandoval et al.

2018). In ω Cen, the numbers of CVs below and above the gap are comparable (Cool et al. 2013), but this result is based on shallower *Chandra* observations (see Table 1), which would have missed most of the faint 47 Tuc CVs. (Deeper *Chandra* observations of ω Cen have been taken, and optical follow-up is now in progress.) For the core-collapsed clusters NGC 6397 (Cohn et al. 2010) and NGC 6752 (Lugger et al. 2017; Cohn et al. 2021), for which the *Chandra* data reach well below $10^{30} \text{erg s}^{-1}$, there are comparable numbers of CVs below and above the period gap. Possible explanations for this relative lack of faint CVs in dense, core collapsed clusters include the destruction or ejection of old (faint) CVs through dynamical encounters, or by a recent burst of dynamical CV formation (making more bright CVs), in an extreme-density phase of core collapse.

1.3 ABs in Globular Clusters

The most abundant class of low-luminosity X-ray source in globular clusters is magnetically active binaries that have enhanced chromospheric and coronal activity, usually due to tidal locking in a close system (van den Berg 2020). Classes of ABs include RS CVn stars (which contain at least one subgiant or giant), BY Dra stars (which contain two main sequence stars), W UMa stars (where one, or both, stars fills its Roche lobe), and sub-subgiants (which lie below the subgiant branch on the CMD). ABs generally have lower X-ray luminosities than CVs; for instance in 47 Tuc, Heinke et al. (2005) found an average $L_X \sim 10^{30} \text{erg s}^{-1}$ for a sample of 60 ABs and $L_X \sim 10^{31} \text{erg s}^{-1}$ for a sample of 22 CVs. In NGC 6397, for which a limiting $L_X \approx 10^{29} \text{erg s}^{-1}$ has been reached, a population of 42 ABs has been detected within the half-light radius (Cohn et al. 2010). Four clusters, 47 Tuc (Heinke et al. 2005; Bhattacharya et al. 2017), M4 (Bassa et al. 2004; Pooley 2016; Bahramian et al. 2020), M22 (Bahramian et al. 2020), and NGC 6752 (Lugger et al. 2017; Cohn et al. 2021) have been observed to a depth of $L_X < 10^{30} \text{erg s}^{-1}$, allowing the detection of significant AB populations.

ABs are expected to be an essentially primordial population in clusters, having evolved from the short-period end of the binary period distribution (Verbunt 2002; van den Berg 2020). This suggests that AB population size should scale with cluster mass, with the proviso that there is variation in the overall binary fraction among clusters. This would imply that for clusters with large AB populations (and without large populations of dynamically formed CVs and LMXBs), X-ray emissivity should be independent of such cluster properties as central density. However, the X-ray emissivities of low-density ($\rho \lesssim 10^2 M_{\odot} \text{pc}^{-3}$) open clusters are substantially higher than those of all but the densest globular clusters (Verbunt 2000; Heinke et al. 2020). Thus, it appears that dynamical interactions may be destroying ABs in globular clusters. This study, along with a comparison to clusters of different masses and densities, will provide a measure of the dependence of the AB population size on cluster properties and thus a measure of the relative importance of primordial and dynamical AB formation and destruction channels.

1.4 The Importance of M4

M4 makes a compelling target for comparison with other nearby, well-studied clusters, given its proximity (both reducing the effect of image crowding and allowing the imaging to go deeper), the moderate density of its core ($\rho_0 \sim 10^4 M_{\odot} \text{pc}^{-3}$) leading to a moderate stellar interaction rate Γ , the presence of an MSP (Lyne

et al. 1988), and the existence of 38 MAVERIC² radio sources, some of which are likely to be MSPs and/or quiescent BH X-ray binaries (Shishkovsky et al. 2020; Zhao et al. 2021). The presence of a confirmed MSP in M4 indicates that dynamical processes are active in its core, which has implications for the CV and AB populations, as discussed above.

Previous *HST* studies to find optical counterparts to *Chandra* sources in M4 are Bassa et al. (2004, 2005) and Pooley (2015, 2016). Using 25 ks of *Chandra* ACIS imaging, and archival *HST* WFPC2 imaging, Bassa et al. (2004, 2005) detected 31 sources and obtained optical identifications for 20 of these. These optical counterparts include two CV candidates, the brighter of which (CX1) now appears to be a neutron star binary (likely a redback MSP; Kaluzny et al. 2012; Pooley 2016), one confirmed MSP, one AGN (CX2, Bassa et al. 2005), one foreground star, and 12 AB candidates. Early results from an analysis of the total of 119 ks of *Chandra* exposure indicate a rich population of X-ray sources of various classes (Pooley 2015, 2016). We have made an additional 28 identifications using the Bahramian et al. (2020) source catalogue and the HUGS photometry database, beyond those found by Bassa et al. (2004), as discussed in Section 5.

2 DATA

2.1 UV and Optical Data

The broad-band UV and optical data come from the Hubble UV Globular Cluster Survey (HUGS; Piotto et al. 2015; Nardiello et al. 2018). This provides 5-band imaging and photometry of M4 in F275W (UV_{275}), F336W (U_{336}), F435W (B_{435}), F606W (V_{606}), and F814W (I_{814}). The former three bands were obtained with the WFC3³, the latter two with the ACS/WFC. Legnardi et al. (2023) have recently corrected the HUGS magnitudes for differential reddening. We employed these corrected magnitudes, which were kindly provided by M. Legnardi (priv. comm.). This corrected photometry uses the KS2 method 1 approach (Nardiello et al. 2018). These data were supplemented by relatively shallow narrow-band F658N ($H\alpha$) and broad-band F625W (R_{625}) ACS/WFC imaging from programme GO-10120 (PI: S. Anderson). These $H\alpha$ and R_{625} frames were reduced using DAOPHOT aperture photometry. Based on these data, (UV_{275} , $UV_{275}-U_{336}$), (U_{336} , $U_{336}-B_{435}$), and (V_{606} , $V_{606}-I_{814}$) CMDs were constructed. In addition an ($H\alpha-R_{625}$, $V_{606}-I_{814}$) colour-colour diagram was generated.

Inclusion of the differential reddening correction makes a substantial improvement in the tightness of the fiducial sequences in the (V_{606} , $V_{606}-I_{814}$) CMD. The effect on bluer CMDs is much less evident, owing to the natural tendency of the $UV_{275}-U_{336}-B_{435}$ filter triplet to produce broad main sequences that provide evidence for the presence of multiple populations. Nonetheless, we now use the differential-reddening-corrected magnitudes for all of the CMDs.

2.2 VLA Data

M4 is one of 25 GCs observed by the *Karl G. Jansky Very Large Array* (VLA) for the *Milky Way ATCA and VLA Exploration of Radio sources In Clusters* (MAVERIC) survey (project codes VLA/13B-014, VLA/15A-100; Shishkovsky et al. 2020) with a total on-source time of 6.9 h. The observations were taken in the most-extended A

Table 3. UV and optical data used in this study

Programme	Observation date range	Inst.	Filter	Exp. (s)
GO-13297	2014-07-05 to 2015-02-17	WFC3	F275W	3086
GO-13297	2014-07-05 to 2015-02-17	WFC3	F336W	1200
GO-13297	2014-07-05 to 2015-02-17	WFC3	F438W	131
GO-10227	2006-03-05	ACS	F606W	110
GO-10775	2006-03-05	ACS	F814W	120
GO-10120	2004-07-26	ACS	F625W	15 ^a
GO-10120	2004-07-26	ACS	F658N	340 ^a

Note.^aWe chose to use to use the single ‘short’ F625W and ‘long’ F658N exposures, as these are contiguous in time, which minimises $H\alpha - R_{625}$ colour offsets that are due to source variability.

configuration, using the C-band receiver. Details of calibration and data reduction processes are described in Shishkovsky et al. (2020). The data were imaged in low (5 GHz) and high frequency (7.2 GHz) sub-bands with beam sizes of $1''.18 \times 0''.08$ and $0''.84 \times 0''.63$, and RMSs of $2.3 \mu\text{Jy beam}^{-1}$ and $2.1 \mu\text{Jy beam}^{-1}$, respectively. The catalogue reports positions, low- and high-frequency flux densities (S_5 and S_7), and a radio spectral index α defined as $S_\nu \propto \nu^\alpha$. In M4, there are 37 radio sources that are detected at the 5σ level.

2.3 Chandra data

Bahramian et al. (2020) used deep *Chandra* ACIS imaging to produce a comprehensive source catalogue of 161 sources in M4, which we use. They labelled each X-ray source with a ‘CXOU_J’ designation that is based on its celestial coordinates. In order to provide a convenient source numbering system, we have extended the ‘CX’ sequence numbering system used by Bassa et al. (2004), ordering the sources by descending L_X (0.5 – 10 keV), as given by Bahramian et al. (2020). We break ‘ties’ by numbering the sources in order of increasing RA. Table 4 gives the correspondence between the ‘CX’ and ‘CXOU_J’ numbering. Bahramian et al. (2020) include marginal sources in their catalogue, clearly identified; we search these error circles as well, but many of them are empty, suggesting that most of these marginal sources are not real.

² Milky Way ATCA and VLA Exploration of Radio sources In Clusters

³ Wide Field Camera 3

Table 4. Source Numbering Convention

CX	CXOU_J	CX	CXOU_J	CX	CXOU_J
1	162334.13-263134.7	61	162344.00-262945.9	115	162335.50-263542.7
3	162338.08-263138.0	62	162330.06-263205.7	116	162319.83-263315.4
4	162334.33-263039.2	63	162342.32-263037.9	117	162339.78-262937.1
6	162338.10-262922.2	64	162340.70-262939.3	118	162351.15-262918.8
7	162345.89-262854.9	65	162340.16-262925.2	119	162337.22-262840.2
8	162331.46-263057.9	66	162323.65-263318.7	120	162331.62-263034.5
10	162335.03-263119.2	67	162323.88-263448.7	121	162349.73-263152.5
11	162332.38-263045.4	68	162352.28-263159.0	122	162347.45-262858.6
12	162338.20-263154.1	69	162317.26-263330.1	123	162314.82-263251.7
13	162334.31-263202.0	70	162329.23-262949.5	124	162328.60-263056.3
14	162326.00-263354.4	71	162322.17-262714.6	125	162335.99-263124.7
15	162336.78-263144.3	72	162335.07-263204.2	126	162352.78-262849.8
16	162333.68-263417.1	73	162340.21-262926.5	127	162334.38-262837.8
17	162335.98-263101.6	74	162333.18-263109.3	128	162342.00-262925.1
18	162345.77-263116.8	75	162331.30-263148.6	129	162343.91-262751.7
19	162328.95-262951.1	76	162341.67-263115.5	130	162335.92-263240.1
20	162336.89-263139.4	77	162341.58-262937.7	131	162333.58-263151.5
21	162334.67-263204.4	78	162338.81-263456.3	132	162338.75-263303.9
22	162333.36-263145.4	79	162348.74-263206.0	133	162330.27-263356.1
24	162342.09-263136.6	80	162335.81-263132.5	134	162336.34-263245.0
25	162333.51-263229.9	81	162331.83-263156.6	135	162328.61-262701.6
26	162338.89-263148.2	82	162334.82-263159.9	136	162345.60-262758.9
27	162333.28-263157.6	83	162337.00-263133.6	137	162342.06-262921.9
28	162334.97-263224.3	84	162336.64-263143.5	138	162347.77-263050.1
30	162328.40-263022.4	85	162336.45-263030.5	139	162332.31-262633.6
32	162335.21-263525.8	86	162341.47-263205.4	140	162347.89-262817.7
33	162334.27-262956.0	87	162335.79-263137.4	141	162341.35-263347.6
34	162349.77-263323.5	88	162339.70-263120.2	142	162350.68-262749.1
35	162352.35-263229.9	89	162335.37-263450.6	143	162333.77-262630.0
36	162346.42-263115.8	90	162324.29-263013.8	144	162337.08-263208.6
37	162346.38-263114.7	91	162333.76-263405.8	145	162345.52-262730.4
38	162337.79-263518.9	92	162344.21-262645.5	146	162331.80-262647.0
39	162336.09-262736.9	93	162346.83-262936.0	147	162328.34-263320.6
40	162334.62-262717.8	94	162328.54-263134.2	148	162340.36-263332.7
41	162352.09-263214.6	95	162338.48-262952.5	149	162347.48-262803.5
42	162335.50-262707.6	96	162317.60-262842.1	150	162340.15-262646.3
43	162326.61-262658.8	97	162339.18-262955.3	151	162344.34-263154.0
44	162352.12-263217.6	98	162322.79-263155.0	152	162316.75-263256.0
45	162351.94-262833.1	99	162351.40-263324.8	153	162334.48-262704.2
46	162338.08-262858.8	100	162330.38-263049.6	154	162332.75-262815.9
47	162352.19-263306.5	101	162334.54-263110.8	155	162329.97-262919.5
48	162342.90-262726.8	102	162339.82-263126.6	156	162331.10-263300.5
49	162352.63-262950.4	103	162319.14-262850.2	157	162325.66-262930.5
50	162350.04-262901.6	104	162334.77-263143.8	158	162325.72-262817.9
51	162352.07-262937.7	105	162327.01-263249.5	159	162340.36-263013.3
52	162322.56-263340.2	106	162323.86-263028.6	160	162328.61-263543.0
53	162335.67-262709.7	107	162319.20-263206.4	161	162337.21-263522.6
54	162329.58-262839.7	108	162320.00-262740.8	162	162350.99-262940.4
55	162333.85-263200.3	109	162320.17-262751.2	163	162346.66-263120.0
56	162339.82-263557.4	110	162333.28-263113.7	164	162318.25-263116.0
57	162330.27-263045.1	111	162319.45-262943.6	165	162325.42-263102.8
58	162345.02-263030.0	112	162328.03-263528.6	166	162336.79-263202.7
59	162323.37-263211.5	113	162351.74-263316.0	167	162340.44-263205.5
60	162336.29-263553.8	114	162320.56-263217.6	168	162331.54-263057.6

3 ASTROMETRY

Given the multi-wavelength datasets used in this study, which were collected at different epochs, it is important to establish a common astrometric reference frame. Since the HUGS positional catalogue is referred to the astrometric system of the *Gaia* Data Release 1 Catalogue (see [Nardiello et al. 2018](#)), we adopted the HUGS object positions as our fundamental reference system. We next computed a boresight correction of the [Bahramian et al. \(2020\)](#)

Chandra source positions to the HUGS/*Gaia* frame based on the offsets of the sources CX1, CX3, CX4, CX10, CX11, CX12, and CX15 from our proposed HUGS counterparts.⁴ These 7 sources are among the brightest in M4; we eliminated CX8 and CX20 from this list, given their larger than typical offsets from the pro-

⁴ The correspondence between the CX source numbering and the [Bahramian et al. \(2020\)](#) source designations is given in Table 4.

Table 5. Measurements of the position of PSR B1620-26

Type	RA-Decl	Epoch	Notes
Timing ^a	16:23:38.199 –26:31:54.34	2015.0	PSR B2629-26
Timing ^b	16:23:38.201 –26:31:54.20	2015.0	PSR B2629-26
VLA ^c	16:23:38.201 –26:31:54.24	2014.5	M4-VLA9
HST ^d	16:23:38.201 –26:31:54.22	2015.0	R0006434
<i>Chandra</i> ^e	16:23:38.199 –26:31:54.23	2015.0	CX12

Notes. ^aPSR position from Thorsett et al. (1999), advanced to 2015.0 using approximate proper motion from Thorsett et al. (1999).

^bPSR position from Thorsett et al. (1999), advanced to 2015.0 using *Gaia* mean cluster proper motion from Vasiliev (2019).

^cSource position from Shishkovsky et al. (2020).

^dSource position from Nardiello et al. (2018).

^eSource position from Bahramian et al. (2020), boresight corrected to HUGS/*Gaia* frame.

posed HUGS counterpart positions. The resulting boresight correction in angular displacement is $\Delta\alpha \cos \delta = -0.099$ arcsec and $\Delta\delta = -0.131$ arcsec. Interestingly, these boresight offsets are nearly precisely what is expected based on the *Gaia*-based proper motion of M4 over the 7.3 year interval between the 2007.7 *Chandra* observations and the 2015.0 HUGS epoch. Vasiliev (2019) gives proper motion components⁵ for M4 of $\overline{\mu_\alpha} = -12.490$ mas yr⁻¹ and $\overline{\mu_\delta} = -19.001$ mas yr⁻¹. These produce shifts of $\Delta\alpha \cos \delta = -0.091$ arcsec and $\Delta\delta = -0.139$ arcsec, agreeing within 0.01 arcsec with our offset.

As a check on the radio–optical–X-ray astrometric alignment, we considered the millisecond pulsar PSR B1620-26, which is detected in the radio, optical, and X-ray. The various measurements of its position in each of the wavelength bands are compared in Table 5. The radio position has been measured both by pulsar timing (Thorsett et al. 1999) and by a direct VLA detection (Shishkovsky et al. 2020). The former measurement has an epoch of 1992.28, and thus must be advanced in proper motion for comparison with the HUGS/*Gaia* frame. We note that the proper motion components given by Thorsett et al. (1999) have a fairly large uncertainty, 8 per cent in RA and 20 per cent in Decl. Vasiliev (2019) have computed much higher accuracy mean proper motion components for M4, based on *Gaia* measurements. We note that the timing position, advanced to epoch 2015.0 using the *Gaia* proper motion, agrees within 0.03 arcsec with the VLA, HST, and *Chandra* positions. Thus, we conclude that there is good astrometric alignment of the radio, optical, and X-ray data with the *Gaia* system.

4 VARIABILITY

4.1 Comparison to M4 Core Project

As part of the M4 Core Project, Nascimbeni et al. (2014) detected 38 variable stars in the core of M4, using deep *HST* WFC3 imaging with the filters F467M and F775W. They provide light curves for each of these variables, demonstrating that 19 of the 38 are eclipsing binaries. Nascimbeni et al. (2014) found that 9 of the 38 variables correspond to *Chandra* sources from the original Bassa et al. (2004) list. We find that an additional 7 of the variables correspond to Bahramian et al. (2020) sources from the extended CX source list. Table 6 provides the cross-IDs for the 16 variable star–X-ray source

Table 6. Cross-IDs with Nascimbeni et al. (2014)

CX	ID ^a	Type ^b	Notes ^c	Present Type	H α ? ^d
3	3236	EB?	BSEQ/TO; CX3	AB	n
8	7864	UNK	Above BSEQ; CX8	AB/??	y
11	8081	UNK	BSEQ; CX11	AB	n
13	3407	cEB	NM; CX13	AB	n
15	3401	cEB	TO; CX15	AB	y
20	3627	EB	MS/BSEQ; CX20	AB	y
21	3153	EB	MS/BSEQ; CX21	AB	y
25	2316	EB	BSEQ; CX25	AB	n
28	2108	dEB	BSEQ; CX28	AB?	n
72	2992	EB?	MS/BSEQ	AB?	n
74	6807	cEB	BSEQ	AB?	y
75	5430	cEB	MS	AB?	n
84	3487	EB	BSEQ	AB	n
86	1001	EB?	BSEQ	AB	–
88	3575	EB	BSEQ	AB	n
94	7202	dEB	BSEQ	AB	n

^aID # from Nascimbeni et al. (2014).

^bBinary type from Nascimbeni et al. (2014). EB = eclipsing binary; c = contact; d = detached; UNK = unknown.

^cNotes from Nascimbeni et al. (2014). BSEQ = binary sequence; NM = non-member.

^dH α excess confirmed in the colour-colour diagram (Fig. 5).

matches. It can be seen that the counterpart types – nearly all AB – inferred from the broad-band photometric properties in the present study are consistent with the binary nature of these objects, as demonstrated by their light curves from Nascimbeni et al. (2014). A number of the objects in Table 6 show strong evidence of H α emission (see Fig. 5), consistent with an active binary nature. Several of the contact eclipsing binaries demonstrate evidence of strange colors in our CMDs (see below), likely due to large variability.

4.2 Variability from HUGS photometry

Each of the HUGS magnitudes has an associated rms (σ), which measures the dispersion over the multiple magnitude measurements. This value may be used as a measure of variability by plotting it against magnitude as in Fig. 1, for U_{336} . In this figure, curves representing the median, the 75th percentile, and the 90th percentile are plotted. Of the variables in Table 6, it can be seen that CX13, CX15, CX25, CX74, CX75, and CX94 register as variables in Fig. 1. The σ –magnitude plot provides an imperfect measure of variability, as it is based on a small number of magnitude measurements (≤ 4). Thus, the light curve sampling is generally incomplete, particularly for the longer period variables. We note that CX1, CX13, CX15, CX74, and CX75, which show the strongest variability signal in Fig. 1, have periods of ≤ 0.3 day. In contrast, CX25 ($P = 1.9$ day) and CX94 ($P = 5.9$ day) show a weaker variability signal. In any case, this plot does provide a useful indication of counterparts which display variability, such as CX1, which is known to have a 0.26 day sinusoidal period.

⁵ The proper motion nomenclature convention used by Vasiliev (2019) is: $\overline{\mu_\alpha} \equiv [d\alpha/dt] \cos \delta$, $\overline{\mu_\delta} \equiv d\delta/dt$.

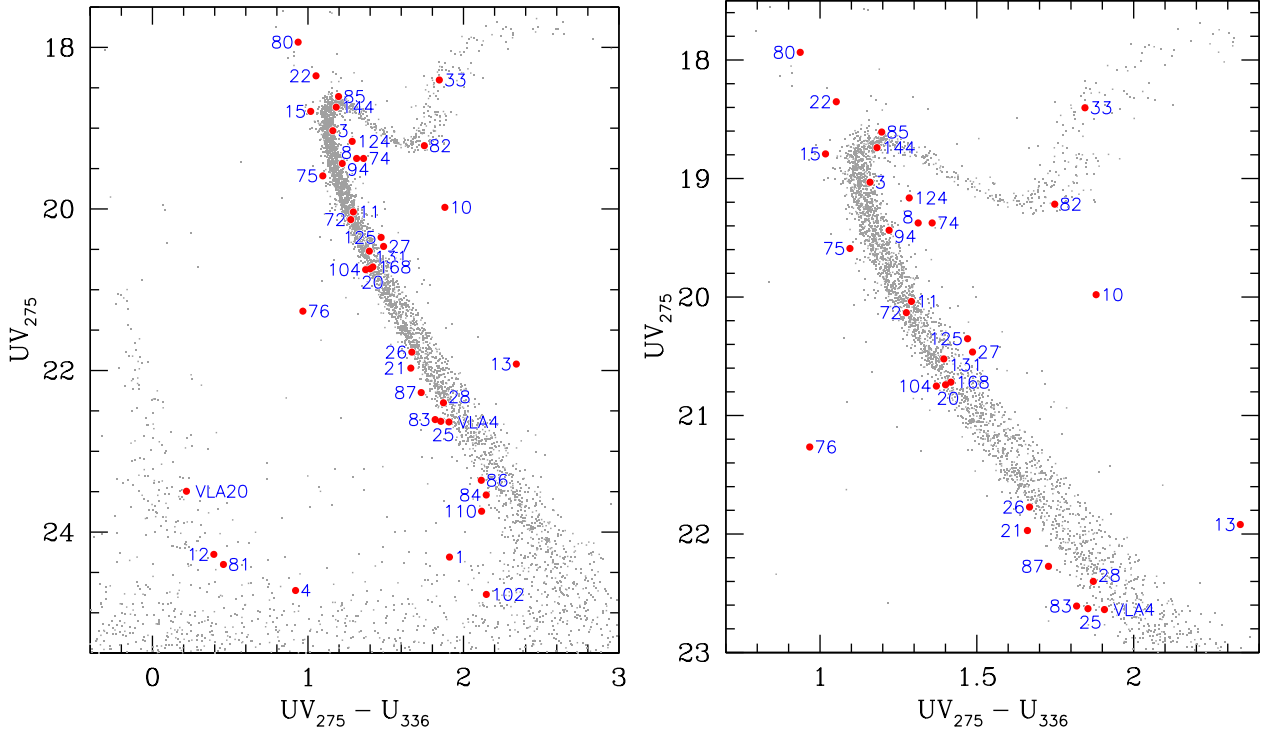


Figure 2. Left panel: Colour-magnitude diagram, based on HUGS photometry in UV_{275} and U_{336} , illustrating the location of candidate counterparts to *Chandra* X-ray sources and to VLA sources without a *Chandra* counterpart. Right panel: Zoom of CMD to show more detail near the MS. CX1 has been interpreted as a neutron star binary (Kaluzny et al. 2012; Pooley 2016). CX12 is the binary counterpart to the millisecond pulsar B1620-26 (Sigurdsson et al. 2003), which is detected as MAVERIC radio source M4-VLA9. The secondary in this system is a low-mass white dwarf. CX4, CX81, and VLA20 have a similar white-dwarf-like presentation to that of CX12. CX4 and CX81 are faint CV candidates. VLA20 is an MSP candidate. CX76 is a bright CV candidate.

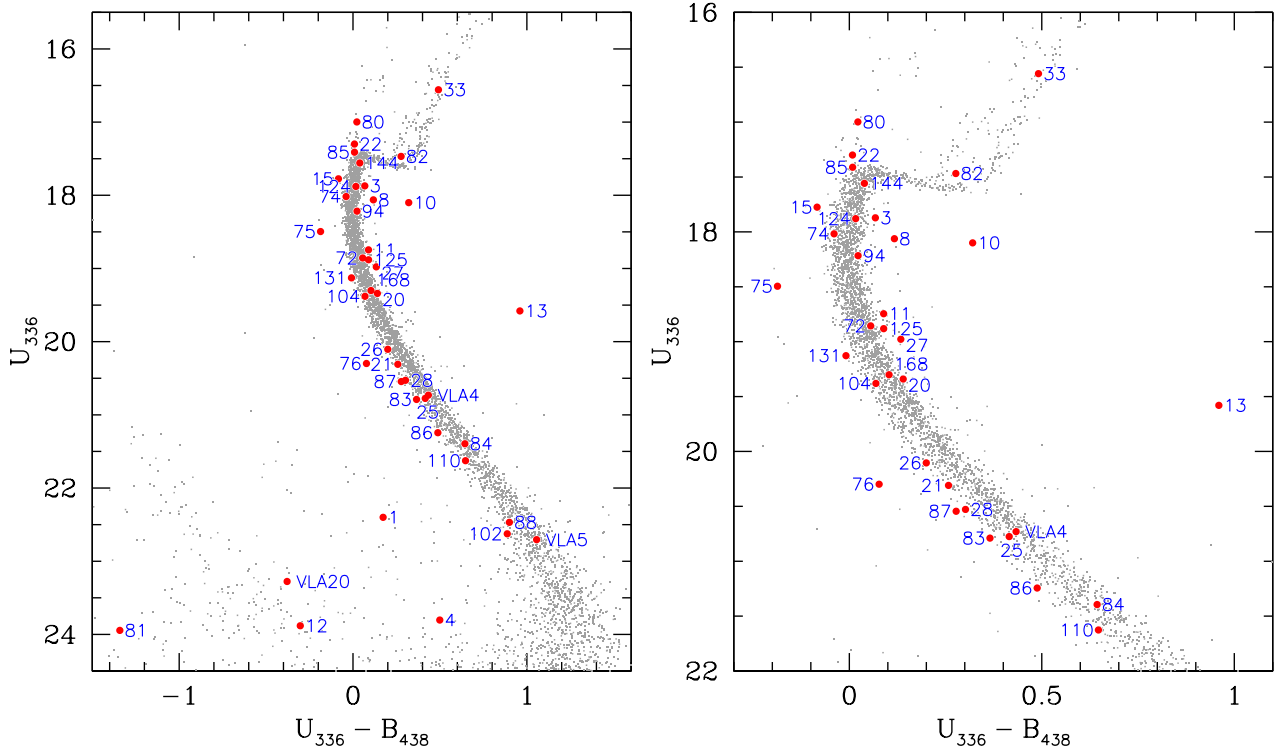


Figure 3. Left panel: Colour-magnitude diagram, based on HUGS photometry in U_{336} and B_{435} , showing the same counterparts as in Fig. 2. Right panel: Zoom of CMD. The counterparts to CX15 and CX75 are consistent with being W UMa-type contact binaries.

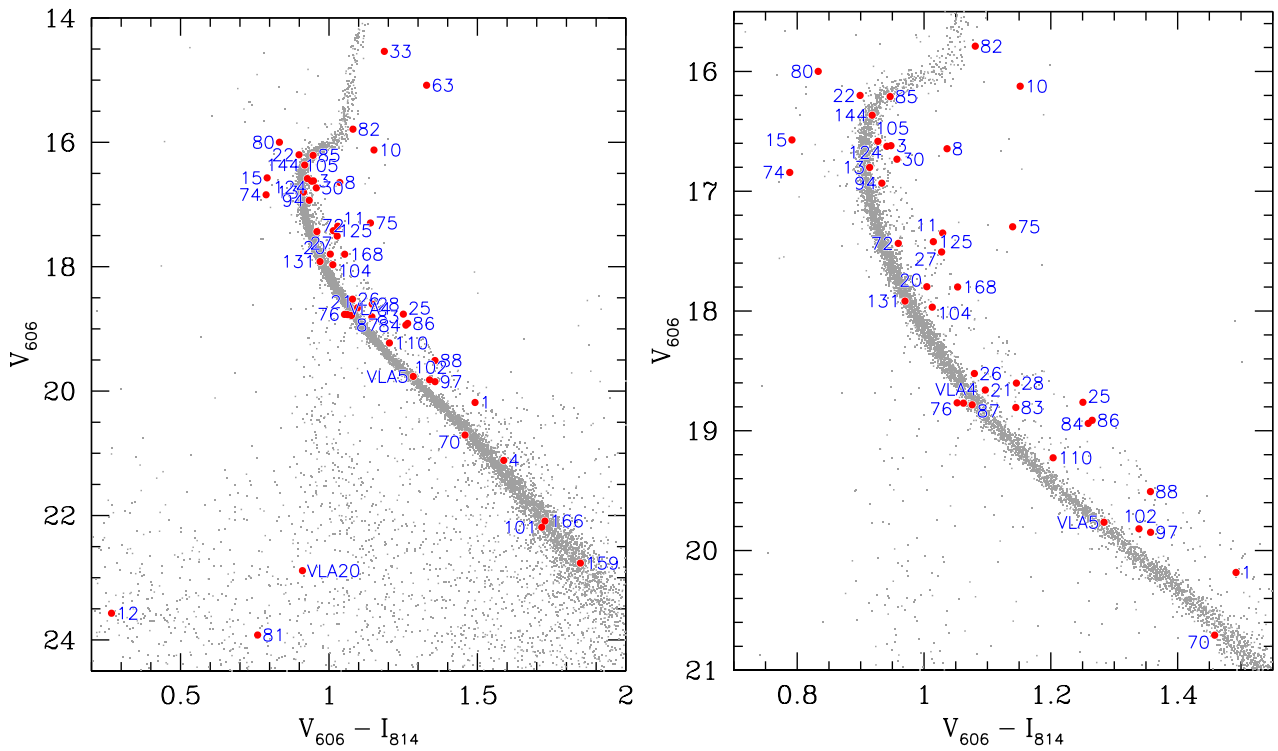


Figure 4. Left panel: Colour-magnitude diagram, based on HUGS photometry in V_{606} and I_{814} , showing the same counterparts as in Fig. 2. Right panel: Zoom of CMD. There are some counterparts that are only detected in these filters, owing to the larger size of the ACS/WFC field relative to the WFC3/UVIS field. Most of the counterparts that lie to the right side of the fiducial sequences are consistent with being ABs.

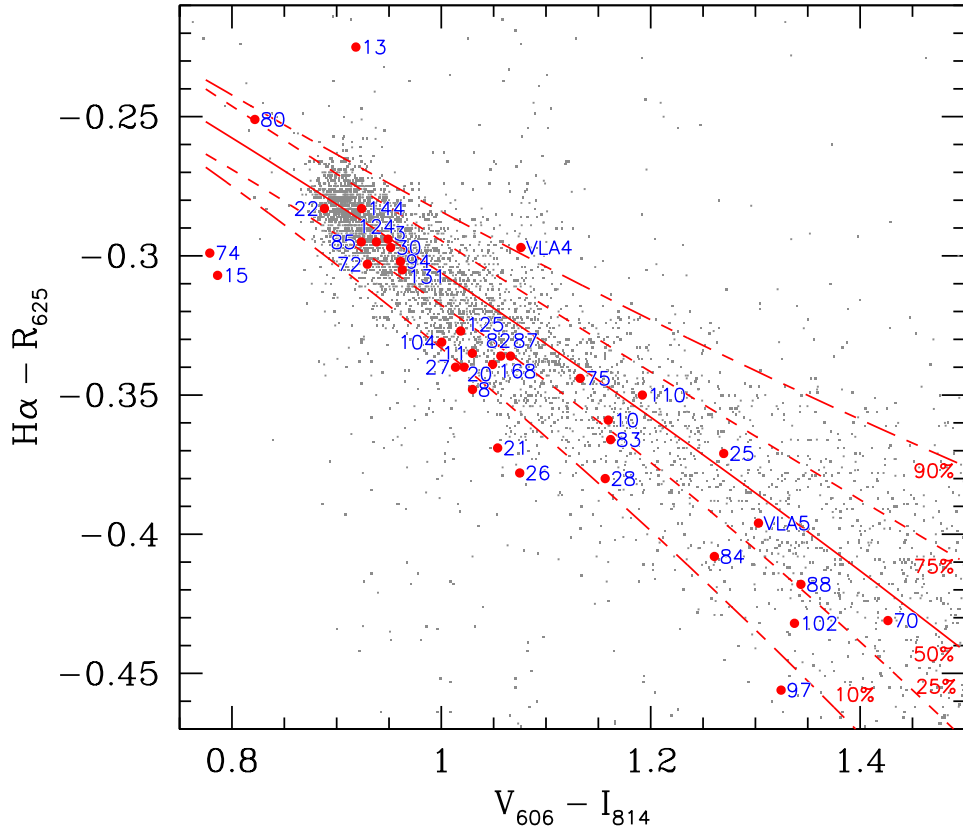


Figure 5. $H\alpha - R_{625}$ index versus $V_{606} - I_{814}$ broad-band colour. The solid curve indicates the median of the $H\alpha - R_{625}$ distribution, the dashed curves indicate the upper and lower quartiles, and the long-short dashed curves indicate the upper and lower deciles. All curves are second-order polynomial fits. Most of the sources fall to the $H\alpha$ -excess side of the median. The sources CX4 and CX101 (large $H\alpha$ excess) and VLA20 (large $H\alpha$ deficit) fall outside the limits of the $H\alpha - R_{625}$ axis.

Table 7. Optical Counterpart Summary

Source ^a	RA, Dec (J2000) ^b	r_{err} (″) ^c	r (′) ^d	L_X (0.5–10 keV) ^e	HUGS #	Offset ^f	Type ^g	Bassa Type ^h	PM ⁱ	Notes
1	16:23:34.125 –26:31:34.90	0.30	0.25	1.54E+32	R0007667	0.14	MSP?/ qLMXB?	CV	0.00	red in $V_{606} - I_{814}$, quite blue in $UV_{275} - U_{336}$ and $U_{336} - B_{435}$, UV-variable; PM likely affected by brighter neighbor
3	16:23:38.074 –26:31:38.18	0.32	0.65	2.89E+31	R0001235	0.08	AB	AB	96.40	slightly red in all CMDs
4	16:23:34.320 –26:30:39.31	0.34	0.91	1.99E+31	R0010636	0.05	CV	CV/AB	96.60	WD seq in $UV_{275} - U_{336}$, blue in $U_{336} - B_{435}$, MS in $V_{606} - I_{814}$, large $H\alpha$ -excess
8	16:23:31.460 –26:30:58.01	0.35	1.02	5.1E+30	R0001877	0.51	SSG??	AB/V52	97.50	SSG in all CMDs, $H\alpha$ -excess
10	16:23:35.031 –26:31:19.38	0.32	0.23	1.63E+31	R0001536	0.04	AB/SSG	AB	97.90	SSG in all CMDs
11	16:23:32.395 –26:30:45.75	0.38	1.01	3.11E+30	R0002030	0.21	AB	–	97.10	on MS in $UV_{275} - U_{336}$, red in $U_{336} - B_{435}$ and $V_{606} - I_{814}$
12	16:23:38.199 –26:31:54.23	0.36	0.76	2.58E+30	R0006434	0.07	MSP	MSP	–	on WD seq in all CMDs
13	16:23:34.310 –26:32:02.20	0.35	0.53	3.02E+30	R0000806	0.15	AB	AB/V49	–	slightly red in $V_{606} - I_{814}$ CMD; PM nonmember, large PM affects other CMD locations
15	16:23:36.781 –26:31:44.49	0.38	0.40	3.66E+30	R0001106	0.18	AB	AB/V48	98.00	BS in all CMDs, $H\alpha$ -excess; eclipsing binary
17	16:23:35.977 –26:31:01.84	0.42	0.54	2.24E+30	–	–	–	–	–	empty error circle near very bright RG
19	16:23:28.915 –26:29:51.08	0.50	2.20	2.48E+30	–	–	–	–	–	out of UVIS FoV; undetected object just outside of error circle in ACS FoV
20	16:23:36.884 –26:31:39.61	0.39	0.39	2.00E+30	R0007345	0.24	AB	AB	97.80	MS in UV CMDs, red in $V_{606} - I_{814}$, $H\alpha$ -excess
21	16:23:34.658 –26:32:04.61	0.38	0.54	1.06E+30	R0005745	0.02	AB	–	98.10	slightly blue in $UV_{275} - U_{336}$, slightly red in $V_{606} - I_{814}$, $H\alpha$ -excess
22	16:23:33.358 –26:31:45.64	0.38	0.47	1.89E+30	R0001090	0.14	AB?/BS	AB	96.70	BS in all CMDs
24	16:23:42.088 –26:31:37.06	0.55	1.54	4.65E+29	R0007270	0.54	Fg?	Amb.	–	not detected in UV_{275} , U_{336} , or B_{435} , extremely red in $V_{606} - I_{814}$
25	16:23:33.492 –26:32:30.14	0.38	1.03	1.15E+30	R0004510	0.26	AB	AB	96.30	slightly blue in $UV_{275} - U_{336}$, on MS in $U_{336} - B_{435}$, red in $V_{606} - I_{814}$
26	16:23:38.882 –26:31:48.22	0.49	0.86	1.15E+30	R0006718	0.37	AB	AB	96.70	MS in $UV_{275} - U_{336}$ and $U_{336} - B_{435}$, red in $V_{606} - I_{814}$, $H\alpha$ -excess
27	16:23:33.272 –26:31:57.94	0.43	0.60	6.45E+29	R0000883	0.29	AB	AB	97.10	red in all CMDs, $H\alpha$ -excess
28	16:23:34.972 –26:32:24.53	0.40	0.86	1.60E+30	R0004784	0.25	AB	AB	97.70	slightly blue in $U_{336} - B_{435}$, red in $V_{606} - I_{814}$
30	16:23:28.378 –26:30:22.33	0.53	1.92	2.11E+30	R0002281	0.10	AB	–	–	out of UVIS FoV; red in $V_{606} - I_{814}$
33	16:23:34.268 –26:29:56.22	0.35	1.62	2.24E+31	R0002524	0.11	AB	V56/Amb.	97.30	red in $V_{606} - I_{814}$; RG in other CMDs
55	16:23:33.835 –26:32:00.57	0.38	0.55	3.13E+30	–	–	–	–	–	empty error circle
57	16:23:30.237 –26:30:45.25	0.48	1.36	2.79E+30	–	–	–	–	–	empty error circle
62	16:23:30.047 –26:32:05.53	0.50	1.28	2.11E+30	–	–	–	–	–	empty error circle
63	16:23:42.332 –26:30:38.47	0.49	1.83	2.00E+30	R0002125	0.12	Fg?	–	–	out of UVIS FoV; to red of RGB in $V_{606} - I_{814}$; <i>Gaia</i> PM indicates nonmember
70	16:23:29.214 –26:29:49.45	0.62	2.18	1.40E+30	R0012571	0.39	AGN	–	–	out of UVIS FoV; MS in $V_{606} - I_{814}$; actual counterpart is likely a radio-bright, optically undetected AGN = M4-VLA1
72	16:23:35.069 –26:32:04.34	0.36	0.53	1.32E+30	R0000770	0.16	AB	–	97.20	MS in UV CMDs, red in $V_{606} - I_{814}$; EB? in Nascimbeni et al. (2014)

Table 7 – *continued* Optical Counterpart Summary

Source ^a	RA, Dec (J2000) ^b	r_{err} (") ^c	r (") ^d	L_X (0.5–10 keV) ^e	HUGS #	Offset ^f	Type ^g	Bassa Type ^h	PM ⁱ	Notes
74	16:23:33.184 –26:31:09.55	0.44	0.60	1.20E+30	R0001710	0.36	AB	–	97.40	red in $UV_{275} - U_{336}$, MS in $U_{336} - B_{435}$, blue in $V_{606} - I_{814}$, H α -excess; cEB in Nascimbeni et al. (2014)
75	16:23:31.308 –26:31:48.79	0.41	0.91	1.17E+30	R0001028	0.22	AB	–	98.00	slightly blue in $UV_{275} - U_{336}$, blue in $U_{336} - B_{435}$, very red in $V_{606} - I_{814}$
76	16:23:41.661 –26:31:15.83	0.46	1.47	1.17E+30	R0008632	0.52	CV	–	98.00	blue in all CMDs
80	16:23:35.811 –26:31:32.69	0.44	0.13	1.07E+30	R0001322	0.15	BS	–	97.90	BS in all CMDs
81	16:23:31.758 –26:31:56.54	0.52	0.86	1.05E+30	R0006301	0.09	CV?	–	–	on WD seq in all CMDs
82	16:23:34.817 –26:32:00.12	0.39	0.46	1.05E+30	R0000841	0.03	RS	–	97.30	RS in $V_{606} - I_{814}$, at SG/RG juncture in other CMDs
83	16:23:36.993 –26:31:33.70	0.44	0.40	9.83E+29	R0007525	0.50	AB	–	96.60	blue in $UV_{275} - U_{336}$, red in $V_{606} - I_{814}$
84	16:23:36.638 –26:31:43.76	0.47	0.37	9.49E+29	R0006962	0.13	AB	–	97.40	blue in $UV_{275} - U_{336}$, red in $V_{606} - I_{814}$
85	16:23:36.444 –26:30:30.62	0.54	1.07	9.28E+29	R0002209	0.36	SG?	–	97.30	SG in all CMDs
86	16:23:41.478 –26:32:05.69	0.47	1.50	8.66E+29	R0005592	0.39	AB	–	97.80	slightly blue in $UV_{275} - U_{336}$ and $U_{336} - B_{435}$, red in $V_{606} - I_{814}$
87	16:23:35.779 –26:31:37.51	0.42	0.15	8.61E+29	R0007423	0.35	AB?	–	97.90	slightly blue in $UV_{275} - U_{336}$ and $U_{336} - B_{435}$, on MS in $V_{606} - I_{814}$
88	16:23:39.710 –26:31:20.49	0.55	1.02	8.30E+29	R0008392	0.49	AB	–	96.50	not detected in UV_{275} , on MS in $U_{336} - B_{435}$, red in $V_{606} - I_{814}$
94	16:23:28.529 –26:31:34.41	0.47	1.49	6.58E+29	R0001298	0.36	AB	–	97.20	slightly red in UV CMDs, red in $V_{606} - I_{814}$
95	16:23:38.506 –26:29:52.71	0.86	1.82	6.14E+29	–	–	–	–	–	poor <i>Chandra</i> detection; out of UVIS FoV; empty error circle in ACS FoV
97	16:23:39.157 –26:29:55.42	0.58	1.85	5.64E+29	R0012464	0.38	AB	–	–	out of UVIS FoV; red in $V_{606} - I_{814}$
100	16:23:30.374 –26:30:49.75	0.82	1.30	4.75E+29	–	–	–	–	–	marginal <i>Chandra</i> detection; empty error circle
101	16:23:34.516 –26:31:10.72	0.55	0.40	4.51E+29	R0008999	0.92	CV?/AB?	–	96.30	out of UVIS FoV; MS in $V_{606} - I_{814}$; large H α excess
102	16:23:39.836 –26:31:26.77	0.50	1.04	4.46E+29	R0007856	0.30	AB	–	98.10	slightly blue in $UV_{275} - U_{336}$ and $U_{336} - B_{435}$, red in $V_{606} - I_{814}$
104	16:23:34.747 –26:31:43.93	0.43	0.21	3.92E+29	R0007155	0.26	AB	–	98.20	slightly blue in $UV_{275} - U_{336}$, red in $V_{606} - I_{814}$
105	16:23:26.986 –26:32:49.43	0.53	2.24	3.72E+29	R0000215	0.60	AB	–	–	out of UVIS FoV; slightly red in $V_{606} - I_{814}$
110	16:23:33.315 –26:31:13.82	0.51	0.54	2.93E+29	R0008707	0.48	AB	–	98.10	blue in $UV_{275} - U_{336}$, MS in $U_{336} - B_{435}$, red in $V_{606} - I_{814}$
120	16:23:31.609 –26:30:34.45	0.57	1.26	1.72E+29	–	–	–	–	–	empty error circle
124	16:23:28.588 –26:30:56.40	0.60	1.60	1.47E+29	R0001915	0.82	AB	–	97.70	red in $UV_{275} - U_{336}$, MS in $U_{336} - B_{435}$, red in $V_{606} - I_{814}$
125	16:23:35.985 –26:31:24.86	0.54	0.22	1.44E+29	R0001440	0.23	AB	–	97.90	red in all CMDs
130	16:23:35.919 –26:32:40.13	0.54	1.14	1.07E+29	–	–	–	–	–	poor <i>Chandra</i> detection; empty error circle
131	16:23:33.595 –26:31:51.73	0.54	0.48	9.55E+28	R0006557	0.51	MS?	–	98.10	poor <i>Chandra</i> detection; very slightly blue in $U_{336} - B_{435}$
132	16:23:38.748 –26:33:03.68	0.48	1.71	9.29E+28	–	–	–	–	–	out of UVIS FoV; empty error circle in ACS FoV
134	16:23:36.365 –26:32:44.85	0.47	1.23	8.50E+28	–	–	–	–	–	empty error circle

Table 7 – *continued* Optical Counterpart Summary

Source ^a	RA, Dec (J2000) ^b	r_{err} (″) ^c	r (′) ^d	L_X (0.5–10 keV) ^e	HUGS #	Offset ^f	Type ^g	Bassa Type ^h	PM ⁱ	Notes
144	16:23:37.092 –26:32:09.13	0.72	0.73	5.68E+28	R0000720	0.84	??	–	97.90	poor <i>Chandra</i> detection – likely false positive; MSTO/SG juncture in all CMDs
151	16:23:44.332 –26:31:54.25	0.90	2.07	5.03E+28	–	–	–	–	–	poor <i>Chandra</i> detection; out of ACS FoV; on edge of UVIS FoV
156	16:23:31.124 –26:33:00.66	0.67	1.73	4.64E+28	–	–	–	–	–	poor <i>Chandra</i> detection; out of UVIS FoV; empty error circle in ACS FoV
159	16:23:40.324 –26:30:13.28	0.82	1.75	4.41E+28	R0011785	0.22	MS?	–	–	poor <i>Chandra</i> detection; out of UVIS FoV; MS in $V_{606} - I_{814}$
166	16:23:36.809 –26:32:02.75	0.50	0.61	3.46E+28	R0005945	0.68	MS	–	95.20	Not detected in UV_{275} or U_{336} ; MS in $V_{606} - I_{814}$
167	16:23:40.450 –26:32:05.76	1.00	1.29	3.16E+28	–	–	–	–	–	poor <i>Chandra</i> detection; empty error circle
168	16:23:31.529 –26:30:57.74	0.35	1.02	2.5E+30	R0009481	0.10	AB	–	96.80	on MS in $UV_{275} - U_{336}$ and $U_{336} - B_{435}$, red in $V_{606} - I_{814}$

Notes. ^aExtension of Bassa et al. (2004) numbering system (sources CX1–CX31) to include the full set of 161 sources reported by Bahramian et al. (2020). Sources are numbered in order of descending X-ray luminosity. Source CX2 has been replaced by sources CX36 and CX37 (which lie outside of the HUGS FoV). Sources CX5 and CX9 from Bassa et al. (2004) have been replaced by CX33. Source CX23 has been replaced by sources CX65 and CX73 (which lie outside of the HUGS FoV). Sources CX29 and CX31 have been dropped, since these were not detected by Bahramian et al. (2020), as discussed in the text.

^bSource position from Bahramian et al. (2020), advanced to 2015.0 using *Gaia* mean cluster proper motion from Vasiliev (2019).

^c95 per cent confidence X-ray error circle radius in arcsec, computed using the prescription of Hong et al. (2005).

^dProjected distance from cluster centre in arcmin.

^eX-ray luminosity in erg s^{-1} , based on a BXA power-law fit from Bahramian et al. (2020).

^fOffset of counterpart from X-ray source position in units of r_{err} .

^gCounterpart type: CV = cataclysmic variable; AB = active binary; RG = red giant; BS = blue straggler; RS = red straggler; SSG = sub-subgiant; MS = main sequence; Fg = foreground; AGN = active galactic nucleus; ? indicates less certain classification. When more than one type is listed, the first type is considered to be the most likely classification.

^hBassa et al. (2004) counterpart type. In addition to the types above, Amb. = ambiguous and V objects are variable stars from Kaluzny et al. (1997) and Mochejska et al. (2002).

ⁱProbability of cluster membership of counterpart in per cent, from HUGS database.

Table 8. Positions and photometry for HUGS counterparts to *Chandra* and VLA sources

CX	HUGS ID	X^a	Y^a	RA, Decl (J2000) ^b		UV_{275}	U_{336}	B_{435}	V_{606}	I_{814}	R_{625}	$H\alpha$
1	R0007667	5366.41	4952.09	16:23:34.128	-26:31:34.92	24.31	22.40	22.23	20.18	18.69	–	–
3	R0001235	4025.24	4869.56	16:23:38.076	-26:31:38.19	19.03	17.87	17.80	16.62	15.67	16.34	16.05
4	R0010636	5301.51	6360.67	16:23:34.319	-26:30:39.30	24.72	23.80	23.30	21.11	19.53	20.51	19.68
8	R0001877	6273.97	5882.37	16:23:31.456	-26:30:58.18	19.38	18.06	17.94	16.65	15.61	16.33	15.98
10	R0001536	5059.89	5345.77	16:23:35.030	-26:31:19.38	19.98	18.10	17.78	16.12	14.97	15.88	15.53
11	R0002030	5956.44	6195.56	16:23:32.391	-26:30:45.81	20.04	18.75	18.66	17.35	16.32	17.14	16.81
12	R0006434	3982.89	4463.69	16:23:38.201	-26:31:54.22	24.28	23.88	24.18	23.57	23.30	–	–
13	R0000806	5303.18	4261.53	16:23:34.314	-26:32:02.20	21.92	19.58	18.62	16.80	15.89	16.62	16.40
15	R0001106	4465.71	4711.67	16:23:36.779	-26:31:44.43	18.79	17.77	17.86	16.57	15.78	16.27	15.97
20	R0007345	4428.86	4835.50	16:23:36.888	-26:31:39.53	20.74	19.34	19.20	17.80	16.79	17.51	17.16
21	R0005745	5186.22	4200.54	16:23:34.658	-26:32:04.61	21.97	20.31	20.05	18.66	17.56	18.30	17.93
22	R0001090	5626.65	4680.86	16:23:33.362	-26:31:45.63	18.35	17.30	17.29	16.20	15.30	15.94	15.65
24	R0007270	2657.62	4892.17	16:23:42.101	-26:31:37.29	27.28	–	–	22.48	19.67	–	–
25	R0004510	5579.87	3553.87	16:23:33.499	-26:32:30.15	22.63	20.78	20.36	18.76	17.51	18.35	17.98
26	R0006718	3753.62	4611.80	16:23:38.875	-26:31:48.37	21.77	20.10	19.90	18.52	17.44	18.30	17.93
27	R0000883	5659.32	4367.21	16:23:33.265	-26:31:58.02	20.46	18.98	18.84	17.51	16.48	17.17	16.83
28	R0004784	5077.11	3695.88	16:23:34.980	-26:32:24.54	22.40	20.53	20.23	18.60	17.46	18.34	17.96
30	R0002281	7320.34	6791.21	16:23:28.377	-26:30:22.28	–	–	–	16.73	15.78	16.52	16.22
33	R0002524	5319.11	7450.74	16:23:34.267	-26:29:56.25	18.40	16.56	16.07	14.54	13.35	–	–
63	R0002125	2579.41	6382.86	16:23:42.330	-26:30:38.42	–	–	–	15.08	13.75	–	–
70	R0012571	7041.22	7619.21	16:23:29.199	-26:29:49.58	–	–	–	20.71	19.25	20.41	19.98
72	R0000770	5047.56	4206.41	16:23:35.066	-26:32:04.38	20.13	18.86	18.80	17.44	16.48	17.16	16.86
74	R0001710	5687.16	5598.71	16:23:33.184	-26:31:09.39	19.38	18.02	18.06	16.84	16.05	16.55	16.25
75	R0001028	6325.24	4598.88	16:23:31.305	-26:31:48.87	19.59	18.49	18.68	17.30	16.16	16.79	16.45
76	R0008632	2806.13	5429.89	16:23:41.664	-26:31:16.06	21.27	20.30	20.22	18.77	17.71	–	–
80	R0001322	4796.12	5008.74	16:23:35.806	-26:31:32.69	17.94	17.00	16.98	16.00	15.17	15.77	15.52
81	R0006301	6172.05	4405.76	16:23:31.756	-26:31:56.50	24.40	23.94	25.29	23.92	23.16	–	–
82	R0000841	5132.58	4314.08	16:23:34.816	-26:32:00.12	19.22	17.47	17.19	15.79	14.71	15.42	15.08
83	R0007525	4388.66	4979.83	16:23:37.006	-26:31:33.83	22.61	20.79	20.42	18.81	17.66	18.53	18.16
84	R0006962	4513.97	4730.06	16:23:36.637	-26:31:43.70	23.54	21.39	20.75	18.94	17.68	18.63	18.23
85	R0002209	4580.37	6585.40	16:23:36.441	-26:30:30.42	18.61	17.41	17.40	16.21	15.26	15.92	15.62
86	R0005592	2873.37	4175.75	16:23:41.467	-26:32:05.59	23.36	21.24	20.76	18.91	17.65	–	–
87	R0007423	4808.10	4889.28	16:23:35.771	-26:31:37.41	22.27	20.54	20.27	18.78	17.71	18.50	18.16
88	R0008392	3475.57	5321.43	16:23:39.693	-26:31:20.34	26.38	22.47	21.57	19.51	18.15	19.14	18.72
94	R0001298	7272.47	4966.17	16:23:28.517	-26:31:34.35	19.44	18.22	18.19	16.93	16.00	16.74	16.44
97	R0012464	3659.59	7476.91	16:23:39.150	-26:29:55.22	–	–	–	19.85	18.49	19.46	19.01
101	R0008999	5235.59	5552.54	16:23:34.513	-26:31:11.21	26.05	26.76	–	22.19	20.47	22.12	21.19
102	R0007856	3424.26	5156.22	16:23:39.845	-26:31:26.87	24.77	22.62	21.74	19.82	18.48	19.42	18.99
104	R0007155	5153.58	4722.83	16:23:34.754	-26:31:43.98	20.75	19.38	19.31	17.97	16.95	17.72	17.39
105	R0000215	7787.65	3058.40	16:23:26.999	-26:32:49.69	–	–	–	16.58	15.66	–	–
110	R0008707	5642.62	5492.74	16:23:33.315	-26:31:13.57	23.74	21.63	20.98	19.23	18.02	18.98	18.63
124	R0001915	7247.12	5939.41	16:23:28.592	-26:30:55.92	19.16	17.88	17.86	16.62	15.68	16.43	16.13
125	R0001440	4736.47	5204.31	16:23:35.982	-26:31:24.97	20.35	18.88	18.79	17.42	16.41	17.18	16.86
131	R0006557	5551.92	4531.87	16:23:33.582	-26:31:51.52	20.52	19.13	19.14	17.92	16.95	17.62	17.32
144	R0000720	4369.60	4097.26	16:23:37.062	-26:32:08.69	18.74	17.56	17.52	16.37	15.45	16.10	15.81
159	R0011785	3257.97	7016.21	16:23:40.333	-26:30:13.41	–	–	–	22.77	20.92	22.45	21.74
166	R0005945	4457.42	4239.40	16:23:36.804	-26:32:03.08	27.91	25.56	24.38	22.09	20.36	21.72	21.19
168	R0009481	6249.93	5893.21	16:23:31.527	-26:30:57.75	20.72	19.30	19.20	17.80	16.75	17.52	17.18
VLA4	R0009986	7293.82	6044.15	16:23:28.455	-26:30:51.78	22.64	20.73	20.30	18.77	17.71	18.52	18.22
VLA5	R0004648	4339.81	3718.55	16:23:37.150	-26:32:23.64	26.04	22.70	21.65	19.76	18.48	19.44	19.04
VLA20	R0005914	3728.37	4316.65	16:23:38.950	-26:32:00.02	23.49	23.28	23.66	22.89	21.98	22.43	22.42

Notes. ^aHUGS star position in frame coordinate system defined by [Nardiello et al. \(2018\)](#).

^bCelestial coordinates are for an observation epoch of 2015.0 (see [Nardiello et al. \(2018\)](#)).

5 CHANDRA SOURCE IDENTIFICATION

As in Cohn et al. (2010), Lugger et al. (2017), and Cohn et al. (2021), we classified objects found in *Chandra* error circles based on their colour-magnitude diagram (CMD) location. In those studies, CVs were distinguished by their blue colours, relative to the main sequence (MS), and their significant $H\alpha - R_{625}$ excesses. ABs were distinguished by their red colours and modest $H\alpha$ excesses. Although deep $H\alpha$ and comparison R_{625} imaging is not available for the present study, we performed aperture photometry on the shallow images in these two bands that are available in the *HST* archive (see Table 3). Thus, our classifications here are based on CMDs that are constructed from the 5-band HUGS photometry, augmented by an $(H\alpha - R_{625}, V_{606} - I_{814})$ colour-colour diagram. In this study, CVs are defined as objects with significant $UV_{275} - U_{336}$ and/or $U_{336} - B_{435}$ excesses (along with evidence of cluster membership, such as a consistent proper motion, $H\alpha - R_{625}$ excess, or location on the main sequence in redder filters), while ABs are identified as generally lying to the right of the main sequence or red giant branch (RGB) in $V_{606} - I_{814}$ colour. $H\alpha - R_{625}$ excesses, where measurable, are taken as additional evidence supporting the CV and AB classifications. Calculating the $H\alpha$ photometric equivalent width (EW) following De Marchi et al. (2010), we see that all $H\alpha$ -excess counterparts except CX4 and CX101 (likely CVs) have $H\alpha$ EW $< 5 \text{ \AA}$, as generally observed for chromospherically active binaries (Beccari et al. 2014; Pallanca et al. 2017). Identifications of stars by Nascimbeni et al. (2014) as eclipsing binaries constitute strong evidence for active binaries (see Section 4.1).

Finding charts in the V_{606} band for the 61 *Chandra* sources that lie within the HUGS field of view are shown in Appendix B, which is included in the supplementary online material. Given its status as the nearest globular cluster, M4 has a very dispersed appearance on the sky. As a consequence, in many cases there is a unique object in each *Chandra* error circle, which makes it a likely counterpart provided that it deviates from the fiducial sequences in the CMDs. Many of the Bahramian et al. (2020) sources lie outside of the HUGS field of view (FoV) and cannot be classified based on their optical properties (except for a few that are bright enough for detection by *Gaia*, see Section 5.6). In a few cases, the source lies within the HUGS FoV, but the error circle is empty.

Table 7 summarises the result of the classification procedure. Only those sources that lie within the HUGS FoV are listed. Classifications are given for 44 confident sources, which includes 16 X-ray sources previously classified by Bassa et al. (2004). We were able to recover most of their 31 X-ray sources. CX29 and CX31, the two lowest luminosity sources in their sample, may represent false positive detections, as the total exposure of 119 ks analysed by Bahramian et al. (2020) is nearly 5 times longer than the 25 ks subset of this exposure analysed by Bassa et al. (2004). Inspection of all three *Chandra* observations does not support the reality of CX29 and CX31, so we removed them from our ‘CX’ list. We also could not confirm the reality of CX5 and CX9 as two separate sources. Bassa et al. (2004) identify these as overlapping sources, separately identified using the `wavdetect` algorithm, but inspection of all three *Chandra* images suggests the X-ray point-spread function is consistent with other sources at this off-axis angle (consistent with Bahramian et al. 2020). We retain CX5/CX9 as a single source, here labeled CX33. However, we identify CX8 as consisting of two separate sources, with a fainter X-ray source (here labeled CX168) located $\sim 1''$ NE of the brighter source; both have secure optical counterparts. We estimate the L_X of CX168 to be 0.5 that of the

brighter object, CX8, based on the numbers of photons in the core of each source, and scale the Bahramian et al. (2020) L_X values.

Additional changes to the CX labelling of the list of 31 sources from Bassa et al. (2004) are given in the footnotes to Table 7. Bahramian et al. (2020) provide a quality flag for each source, indicating whether the detection is ‘poor,’ ‘marginal,’ or ‘confident,’ where poor detections have a false detection probability of ≥ 1 per cent. We have indicated the marginal and poor detections in the notes column of Table 7. Six of these have empty error circles, and 3 have stars with no unusual properties (likely chance coincidences); most likely, few or none of these are real X-ray sources.

Broad-band CMDs that show the objects listed in Table 7 are presented in Figs. 2–4. The $(H\alpha - R_{625}, V_{606} - I_{814})$ colour-colour diagram is presented in Fig. 5. Table 8 gives the positions and photometry for each of the counterparts listed in Table 7 and plotted in Figs. 2–5.

5.1 Compact Object Binary Candidates

Several of the proposed counterparts show evidence of being a binary containing either a white dwarf (WD) or neutron star (NS).

Bassa et al. (2004) identified a $V=17.37$ star as the counterpart of CX1, which they suggested was a CV. However, they also noted the poor astrometric match (about 2σ away). Kaluzny et al. (2012) used the HST analysis of Anderson et al. (2008) to instead identify another, fainter star ($V=20.65$) as the likely counterpart to CX1, bolstered by the clear sinusoidal variation of the fainter star in both ground-based and HST observations, as well as variation in the *Chandra* X-ray lightcurve. The sinusoidal variation suggests a 0.2628 (preferred), or 0.5256 (for ellipsoidal variation), day orbital period. Kaluzny et al. (2012) argued for a neutron star (and likely radio pulsar) nature of the primary, based on the X-ray/optical flux ratio, and the lack of a strong UV excess and long-term optical or X-ray variations, as would be expected from an X-ray bright CV. We find that CX1 shows strong evidence for variability in U_{336} , based on the rms of its HUGS magnitude (see Fig. 1), consistent with the optical variability found by Kaluzny et al. (2012). We do not detect CX1 in the radio (Section 5.9), but as the RMS of our VLA images only reaches the mean flux (extrapolated to 5 GHz, assuming a spectral slope of -1.9) of the best-fit lognormal luminosity distribution for MSPs of Bagchi & Lorimer (2011), we cannot constrain the presence of a pulsar. The evidence from Kaluzny et al. (2012) indicates that CX1 is probably an MSP.

CX4 was classified as a likely CV by Bassa et al. (2004), based on its high X-ray/optical flux ratio (as its CMD location on the main sequence in $V_{606} - I_{814}$ does not point to a definitive classification). We find CX4 to be quite blue in both UV CMDs, reaching the WD sequence in $UV_{275} - U_{336}$, and to have a proper motion consistent with the cluster, confirming its classification as a CV. Furthermore, it has a strong $H\alpha - R_{625}$ excess. Its main sequence position in $V_{606} - I_{814}$ allows us to estimate the mass of the companion star (which must provide most of the optical light) as $\sim 0.5 M_{\odot}$ (using an isochrone of Dotter et al. 2007, assuming an age of 12.8 Gyr from Hansen et al. 2004, and taking $(m - M)_V = 12.8$ from Harris 1996), which suggests an orbital period of roughly 4.5 hours (Howell et al. 2001).

CX12 is a well-studied MSP with a white dwarf companion (and also a planet-mass companion in a wide orbit; Thorsett et al. 1999; Sigurdsson et al. 2003). It lies on the WD sequence in all three CMDs. Its radio properties are discussed in Section 5.9, and its X-ray properties in Appendix A.

CX76 is a newly identified X-ray source in Bahramian et al.

(2020). We here identify it with a moderately bright optical counterpart that is marginally blue compared to the main sequence in $V_{606}-I_{814}$, and progressively bluer in bluer filters. Its CMD locations suggest that it is a CV with a low-mass donor star (we may estimate $\sim 0.65 M_{\odot}$, using the [Dotter et al. 2007](#) isochrone as above), with an orbital period of order 5.5 hours.

CX81 lies on the WD sequence in all broad-band CMDs. It is too faint to be detected in $H\alpha-R_{625}$. The HUGS data do not provide a proper motion estimate (as it is only barely detected), but comparison of the 2008 and 2014 images suggests it moves with the cluster stars, and thus is a cluster member. Given its very blue $V_{606}-I_{814}$ colour, we infer this is likely to be a CV below the period gap, though an MSP with a WD companion is possible (however, in Section 6 below, we show that its X-ray colours and luminosity do not match other cluster MSPs).

CX101 has a very faint candidate counterpart, which lies on the main sequence in $V_{606}-I_{814}$, but appears to show a very strong $H\alpha$ excess, ~ 0.4 magnitudes. Such an excess is larger than typical for chromospherically active stars (e.g. [Beccari et al. 2014](#)), making this star a candidate CV. However, the star is near the detection limit, and we do not fully trust the photometry here; if the excess is not real, this star may not be the true counterpart.

5.2 Chromospherically active binary candidates

ABs often differ from average cluster stars in several ways; lying on the binary sequence above the MS (this sequence includes objects that lie up to 0.75 mag above the MS in the $(V_{606}, V_{606}-I_{814})$ CMDs, which represents the equal-mass limit); showing an $H\alpha-R_{625}$ excess (lower quartile in Fig. 5); showing optical variability identified by [Nascimbeni et al. \(2014\)](#); showing variability in the U_{336} filter (Fig. 1, upper quartile). ABs may not show any of these, but the likelihood of a chance coincidence of an X-ray source with an unremarkable star is significant, while the likelihood of matching stars in one of these categories is small (Section 5.4), so we identify counterparts with any of the above characteristics as ‘AB’ and potential counterparts without these as ‘AB?’.

The majority of AB counterparts lie on the binary sequence in the $(V_{606}, V_{606}-I_{814})$ CMD. These objects include CX3, CX11, CX20, CX21, CX25, CX26, CX27, CX28, CX30, CX72, CX83, CX84, CX86, CX88, CX94, CX97, CX102, CX104, CX105, CX110, CX124, CX125, and CX168. Most of these are verified proper motion members, though CX30, CX97, and CX105 lack UVIS data (so have no proper motion measurement). The colour-magnitude diagram comparing $H\alpha-R_{625}$ and $V_{606}-I_{814}$ identifies high-confidence (>90 per cent) $H\alpha$ emission from CX20, CX21, CX26, CX27, and CX97, and lower-confidence (>75 per cent) $H\alpha$ from CX11, CX28, CX72, CX82, CX83, CX84, CX102, CX104, CX125, and CX168.

An additional four objects, CX8, CX10, CX24, and CX75, fall significantly further above the binary sequence region. CX8 and CX10 fall in the sub-subgiant region, while CX75 falls below this region. These three objects are secure proper-motion members, while the proper-motion membership status of CX24 is undetermined (likely a foreground star).

CX15, CX74, and CX75 are identified, via their light curves, as likely contact eclipsing binaries with orbital periods of 0.3 day by [Nascimbeni et al. \(2014\)](#). While their HUGS $V_{606}-I_{814}$ colour offsets from the MS appear large – CX15 and CX74 are to the blue of the MS and CX75 is to the red of the MS – it appears likely that these offsets are a consequence of unrepresentative sampling of the light curves for these short-period binaries. [Kaluzny et al. \(2013\)](#)

and [Nascimbeni et al. \(2014\)](#) have presented CMDs for M4, based on high-time-resolution sampling of the light curves that allows the determination of appropriate mean colours. In both the $B-V$ CMD ([Kaluzny et al. 2013](#)) and the F467M – F775W CMD ([Nascimbeni et al. 2014](#)), all three counterparts fall very close to the MS. The largest deviation is that of CX74, which is on the binary sequence just to the red of the MS in F467M – F775W. We thus classify all three objects as ABs, of the W UMa type, based on their identification as contact eclipsing binaries with variability amplitudes of over 0.3 magnitudes, short 0.3 day orbital periods, light curve morphology, lack of flaring, and approximate agreement with the [Rucinski \(1995\)](#) relation between absolute magnitude, period, and colour for W UMa variables.

CX33 (formerly CX5/CX9), to the red of the giant branch in $V_{606}-I_{814}$ but a clear proper motion member, has been associated with variable V56 by [Kaluzny et al. \(2013\)](#). They note that it shows clear evidence of luminosity and velocity variability, which supports its identification as a binary, and thus an (RS CVn-type) AB.

CX13 is a proper motion nonmember, a contact eclipsing binary with a 1-mag variation amplitude ([Nascimbeni et al. 2014](#)). Although it is on the MS in the $(V_{606}, V_{606}-I_{814})$ CMD (Fig. 4), it is well to the red of the MS in both $B-V$ ([Kaluzny et al. 2013](#)) and F467M – F775W ([Nascimbeni et al. 2014](#)). Since these two studies provide high-time-resolution sampling of the 0.3 day period light curve, they provide a more reliable measure of the mean colour of this star than does the HUGS database for which the V_{606} and I_{814} magnitudes are measured at different orbital phases. While this star is clearly quite red, the HUGS measurements of its UV_{275} , U_{336} , and B_{435} magnitudes appear to be too faint, likely as a result of its large proper motion. Therefore we performed aperture photometry for this star, in the UVIS filters, choosing several surrounding stars to serve as photometric standards. The determined aperture UVIS magnitudes for CX13 are given in Table 8 and plotted in Figs. 2 and 3.

In the bluer broad-band colours, $UV_{275}-U_{336}$ and $U_{336}-B_{435}$, AB candidates may fall either to the right or left of the MS, presumably indicating the degree of UV emission, which increases with chromospheric activity. The $UV_{275}-U_{336}$ colour is most sensitive to chromospheric UV emission. Examination of Fig. 3 indicates that in $U_{336}-B_{435}$, most of the AB candidates fall near the MS, with the fainter ones lying to the blue side of the MS. In Fig. 2, a number of the AB candidates lie distinctly to the blue of the MS in $UV_{275}-U_{336}$, including CX21, CX25, CX83, CX84, CX87, CX102, CX104, and CX110. We take this as an indication of enhanced chromospheric activity. Examples of AB candidates that fall on the $V_{606}-I_{814}$ binary sequence or in the sub-subgiant region and do not show significant UV excesses are CX3, CX8, CX10, CX11, CX20, CX26, CX27, CX28, CX86, CX94, and CX168.

5.3 Summary of source identifications

For clarity, we summarise our 24 new confident optical identifications with *Chandra* X-ray sources from the current study. We identify 19 new confident ABs (CX11, CX21, CX30, CX72, CX74, CX75, CX83, CX84, CX86, CX88, CX94, CX97, CX102, CX104, CX105, CX110, CX124, CX125, and CX168). We identify one new confident CV (CX76), one new confident blue straggler (CX80), two new confident subgiants (CX82 and CX85), and one new confident foreground or background star (CX63). We also suggest one new candidate AB (CX87) and two new candidate CVs (CX81 and CX101). We also note two main sequence stars that are the only stars that fall in the X-ray error circles (CX70 and CX166); these are

Table 9. Chance coincidence analysis.

Population	N_{obs}^a	N_{pred}^b	Excess ^c	Significance (σ) ^d
MS	17	10.0	7.0	1.7
BSEQ	28	0.8	27.2	6.3

Notes. ^aObserved number of population members in all error circles.
^bPredicted number of population members in all error circles.
^cExcess of observed versus predicted number in all error circles.
^dSignificance of excess expressed as a Gaussian-equivalent σ level, based on [Gehrels \(1986\)](#) statistics.

likely chance superpositions. CX70 has a radio counterpart (VLA1) and is therefore likely an AGN that is unrelated to the main sequence star in the X-ray error circle.

We also summarise the previous 16 confident optical identifications from [Bassa et al. \(2004, 2005\)](#). These include 10 ABs (CX3, CX8, CX10, CX15, CX20, CX25, CX26, CX27, CX28, and CX33), one CV (CX4), one MSP (CX12), one possible MSP (CX1), two foreground or background stars (CX13 and CX24), and one AGN (CX2). While [Bassa et al. \(2004\)](#) classified CX22 as an AB, we now consider it to be a candidate AB, given its location in the blue straggler region of all CMDs. CX8 is also a VLA source (VLA31), and is discussed further in § 5.9.

5.4 Evaluating the probability of chance superpositions

Given the substantial number of apparent ABs in *Chandra* error circles, we have investigated the expected number of chance superpositions of such stars with error circles. We followed the approach of [Cohn et al. \(2021\)](#), who used the GLUE software package ([Beaumont et al. 2015](#); [Robitaille et al. 2017](#)) to define regions in the $V_{606} - I_{814}$ CMD. This is illustrated in Fig. 6, where MS and binary sequence (BSEQ) groups are selected. The BSEQ region has been extended to include sub-subgiant stars. We then determined the number of stars in these groups inside X-ray error circles, and the radial density profiles of these groups. The latter were used to compute the local densities of group members at the locations of each source and thus to predict the number of chance superpositions in each error circle. The total numbers of observed and predicted objects in the error circles were calculated along with the significance of the excesses, based on [Gehrels \(1986\)](#), using the formulae presented by [Cohn et al. \(2021\)](#). The results of this analysis are summarised in Table 9. There is an insignificant 1.7σ excess of 7.0 MS stars in the error circles. Of these excess ‘MS’ stars, three are actually other types. These stars, and their types from Table 7, are: CX4 (CV), CX13 (AB), and CX87 (AB?). Reducing the number of MS stars in error circles to 14 results in an excess of 4.0 stars over the expected background of 10.0 stars, which has a significance level of 0.9σ . In contrast, the excess of 27.2 BSEQ stars in the *Chandra* error circles registers at a 6.3σ level, strongly indicating that the majority of the AB and AB? identifications are the likely counterparts to the *Chandra* sources.

5.5 X-ray/optical flux ratio

Another piece of evidence that can help classify the nature of X-ray sources is comparison of X-ray luminosity vs. absolute magnitude. As discussed by [Verbunt et al. \(2008\)](#), quiescent LMXBs can reach the highest X-ray/optical ratios, followed by CVs, with ABs producing relatively little X-ray flux compared to their optical flux. The dividing line between CVs and ABs (or, rather, the

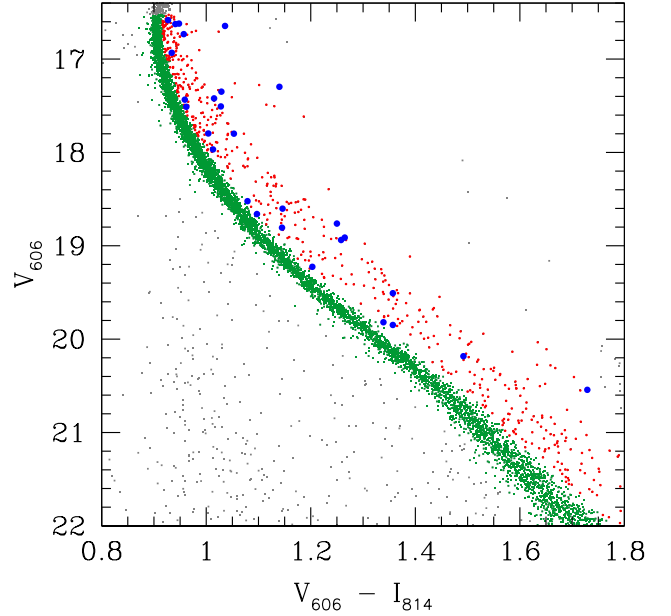


Figure 6. Stellar population selection using GLUE software. Colour key: green–MS; red–BSEQ; grey–all other stars. BSEQ stars within *Chandra* error circles are shown as blue dots.

ceiling for ABs, since CVs can be X-ray dim in quiescence) is not firmly settled; while the line $\log L_X(0.5-2.5 \text{ keV}) = 34.0 - 0.4 M_V$ seems to bound ABs empirically in globular clusters, the line $\log L_X(0.5-2.5 \text{ keV}) = 32.3 - 0.27 M_V$ seems to bound ABs in the solar neighbourhood ([Verbunt et al. 2008](#)).

We create a plot of 0.5–2.5 keV X-ray luminosity vs. M_V , for our M4 sources. We use the F606W HUGS magnitudes and an extinction-corrected distance modulus of 12.82 ([Harris 1996, 2010](#) edition) to derive M_V . The small shift from using F606W is not important for our purpose. Similarly, small variations due to differential reddening are not important to the total extinction correction. We extrapolate the 0.5–2.0 keV L_X values of [Bahramian et al. \(2020\)](#) to the 0.5–2.5 keV band (note that reddening, in the form of N_H , is included in their X-ray spectral fitting). We find (Fig. 7) that all but four X-ray sources with HUGS F606W magnitudes lie below both empirical AB upper limit lines. The exceptions were identified above as a CV (CX4), a CV candidate (CX81), an MSP (CX12 = pulsar M4 A), and a candidate MSP or qLMXB (CX1). All other objects are consistent with an AB nature. However, we do not take this as evidence that, e.g., the CV candidate CX76 is actually an AB, as CVs can have moderately bright optical counterparts without being X-ray bright. The X-ray/optical luminosity ratio plot generally supports our classifications of *Chandra* sources presented in Table 7, as these are primarily found to be ABs.

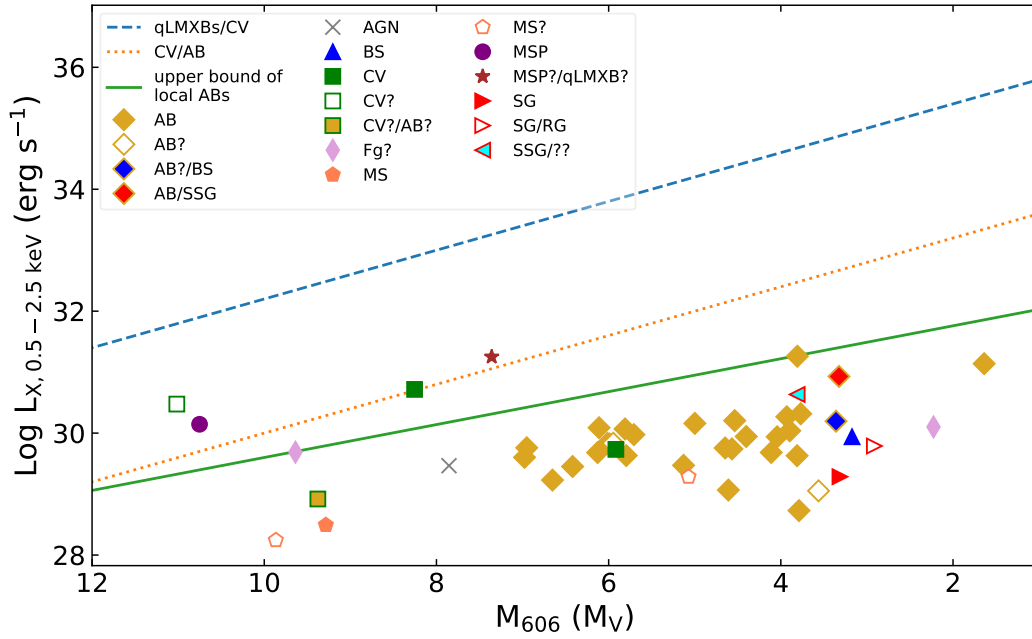


Figure 7. 0.5–2.5 keV X-ray luminosity plotted against M_V , estimated from HUGS F606W magnitudes. The lines suggested by [Verbunt et al. \(2008\)](#) are plotted; the highest separates X-ray bright quiescent LMXBs from CVs, while the others are different suggested separating lines between (X-ray brighter) CVs, and ABs. Most of our counterparts lie below all these lines, consistent with ABs, matching our classifications.

Table 10. *Gaia* counterparts to 17 X-ray sources

ID ^a	RA, Dec (J2000) ^b (hhmmss.sss, ddmms.ss)	Dist ^c (arcmin)	L_X ^d (0.5–10 keV)	Type ^e	<i>Gaia</i> ID ^f	Parallax (mas)	PM ^g (mas yr ⁻¹)	BPmag ^h (mag)	RPmag ^h (mag)	Offset ⁱ (arcsec)	Note ^j
7	16:23:45.854 –26:28:55.04	3.55	4.71E+30	–	6045466468307366656	3.42 ± 0.01	60.74 ± 0.02	12.892 ± 0.003	11.672 ± 0.004	0.47	Fg
18	16:23:45.758 –26:31:16.89	2.38	1.13E+30	–	6045465506234526592	0.62 ± 0.06	23.28 ± 0.10	16.987 ± 0.023	15.801 ± 0.021	0.11	Member
30	16:23:28.378 –26:30:22.33	1.92	2.11E+30	AB	6045466159069806464	–	–	16.534 ± 0.009	15.197 ± 0.007	0.07	–
32	16:23:35.202 –26:35:26.08	3.89	4.86E+31	–	6045463169761296000	0.09 ± 0.65	0.47 ± 1.11	20.335 ± 0.062	19.269 ± 0.044	0.22	Bkg?
33	16:23:34.268 –26:29:56.22	1.62	2.24E+31	AB	6045466502667300096	0.48 ± 0.02	22.01 ± 0.05	14.967 ± 0.005	13.374 ± 0.005	0.04	Member
38	16:23:37.768 –26:35:19.13	3.81	9.11E+30	–	6045464647232984960	–	–	–	–	0.22	–
42	16:23:35.533 –26:27:08.41	4.42	7.95E+30	–	6045478459856719104	0.41 ± 0.05	5.11 ± 0.08	17.089 ± 0.004	15.421 ± 0.005	0.46	Field
63	16:23:42.332 –26:30:38.47	1.83	2.00E+30	Fg?	6045466262148847232	2.83 ± 0.03	7.78 ± 0.05	15.631 ± 0.004	13.810 ± 0.004	0.16	Fg
65	16:23:40.165 –26:29:25.61	2.40	1.70E+30	–	6045466330858826752	0.37 ± 0.15	23.01 ± 0.23	18.014 ± 0.149	16.789 ± 0.096	0.46	Member
69	16:23:17.264 –26:33:30.33	4.47	1.41E+30	–	6045464436777542784	1.23 ± 0.19	6.51 ± 0.30	19.784 ± 0.136	17.187 ± 0.010	0.15	Fg
70	16:23:29.214 –26:29:49.45	2.18	1.40E+30	MS?	6045466193420208256	1.80 ± 1.47	23.66 ± 2.40	–	–	0.26	Member
90	16:23:24.277 –26:30:13.79	2.77	7.26E+29	–	6045477910092876800	0.75 ± 0.19	22.69 ± 0.30	17.972 ± 0.433	16.117 ± 0.074	0.32	Member
91	16:23:33.777 –26:34:05.89	2.57	7.23E+29	–	6045464922118910720	0.57 ± 0.07	23.18 ± 0.12	17.465 ± 0.011	16.075 ± 0.006	0.05	Member
97	16:23:39.157 –26:29:55.42	1.85	5.64E+29	AB	6045466330859725184	0.46 ± 0.48	23.27 ± 0.70	–	–	0.22	Member
98	16:23:22.810 –26:31:55.58	2.80	4.91E+29	–	6045466021630961408	0.60 ± 0.07	22.38 ± 0.12	17.303 ± 0.009	15.959 ± 0.008	0.09	Member
105	16:23:26.986 –26:32:49.43	2.24	3.72E+29	AB	6045465746742763264	0.90 ± 0.08	22.78 ± 0.12	16.856 ± 0.050	15.187 ± 0.134	0.32	Member?
124	16:23:28.588 –26:30:56.40	1.60	1.47E+29	AB	6045466090350294784	0.40 ± 0.07	22.47 ± 0.10	16.850 ± 0.018	15.597 ± 0.012	0.47	Member

Notes: ^aSource numbering in this work. See Table 7.

^bSource position from Bahramian et al. (2020), advanced to 2015.0 using *Gaia* mean cluster proper motion from Vasiliev (2019).

^cSource distance from the cluster centre in arcmin, from Bahramian et al. (2020).

^dX-ray luminosity in erg s⁻¹, based on a BXA power-law fit from Bahramian et al. (2020).

^eOptical counterpart type identified by HUGS photometry. See Table 7.

^f*Gaia* unique source identifier in DR3.

^gTotal proper motion, from *Gaia* DR3.

^hMean magnitudes from *Gaia* DR3.

ⁱOffset of *Gaia-Chandra* match in arcsec.

^jAssociation with M4, based on parallax and proper motion. Member: considered true member of M4; Fg: foreground source; Bkg: background source; Field: Field star. ? indicates less certain classification.

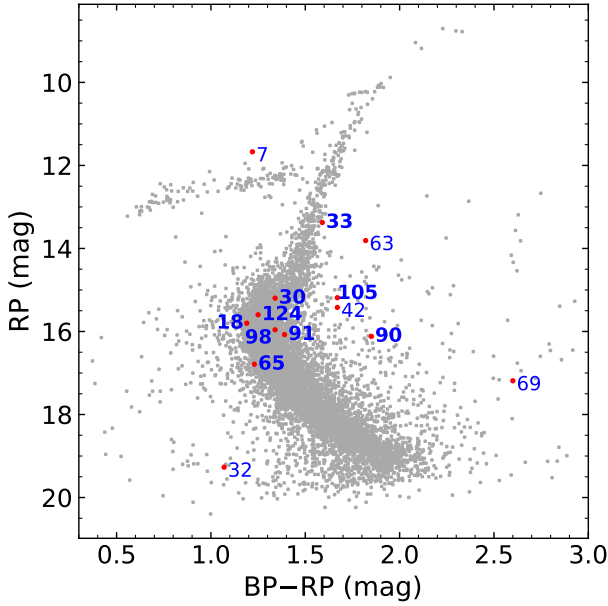


Figure 8. Colour-magnitude diagram of M4, based on *Gaia* DR3 photometry. The counterparts to 10 X-ray sources in the outer region of M4 are highlighted as red dots with CX IDs labelled, while labels in boldface indicate true M4 members.

5.6 *Gaia-Chandra* matches

Since the HUGS FoV only covers the central ~ 1.7 arcmin radius region of M4, whereas the half-light radius of M4 is ~ 4.3 arcmin (Harris 1996, 2010 edition), many X-ray sources in Bahramian et al. (2020) are not covered by HUGS. Therefore, we used *Gaia* Data Release 3 (DR3; Gaia Collaboration et al. 2016, 2022) to seek potential optical counterparts in the outer regions of the cluster.

We first selected X-ray sources with distances from the cluster centre > 1.5 arcmin, and then cross-matched those X-ray sources with DR3 sources (positions at 2016.0 epoch) in TOPCAT (Taylor 2005). Given that the typical centroiding uncertainties of those X-ray sources are less than 0.5 arcsec (see Bahramian et al. 2020), we thus limited the matching offsets to less than 0.5 arcsec, and found 17 *Gaia-Chandra* matches (Table 10, Figure 8). The small proper motion components for M4 of $\overline{\mu_\alpha} = -12.490 \text{ mas yr}^{-1}$ and $\overline{\mu_\delta} = -19.001 \text{ mas yr}^{-1}$ (Vasiliev 2019) produce only small shifts ($\Delta\alpha \cos \delta = -0.012$ arcsec and $\Delta\delta = -0.019$ arcsec) over the one-year interval between the epochs of X-ray positions (advanced to 2015.0 epoch; see Table 7) and *Gaia* DR3 positions. Boresight corrections between these epochs are not needed for finding *Gaia* counterparts. To check for chance coincidences, we shifted the X-ray sources by 5 arcseconds in different directions and redid the cross-matching process correspondingly. We find 3 matches on average per shift, indicating of order three of our matches are likely spurious, while roughly 14 of them are real. Ten of these matches have proper motions (see Table 10) within 2 sigma of the proper motion of M4 (22.7 mas yr^{-1} , with a central proper motion dispersion of $\sim 0.5 \text{ mas yr}^{-1}$), and we therefore suggest these stars (CX 18, 33, 65, 70, 90, 91, 97, 98, 105, and 124) are members of M4. In addition, we checked parallaxes in Gaia Collaboration et al. (2022) and distances in Bailer-Jones et al. (2021) for those counterparts, and found that all of these likely matches have parallaxes that are consistent within 2 sigma of the distance to M4 ($1.85 \pm 0.02 \text{ kpc}$, Baumgardt et al.

2021; but cf. Harris 1996, 2010 revision which gives 2.2 kpc, which would not change this result), except for the counterpart to CX105, which has a parallax of $0.90 \pm 0.08 \text{ mas}$. Considering both the total proper motion, and proper motions in RA and Dec, of the CX105 counterpart are consistent with M4, we suggest it is probably an M4 member. The relatively high parallax might be a consequence of intrinsic motion of the binary stars, as suggested by its moderately high *Gaia* EDR3 RUWE value of 1.225 (Stassun & Torres 2021). On the other hand, the proper motions and (large) parallaxes of CX7, CX63, and CX69 suggest they are foreground stars. CX32 is likely a background AGN (its proper motion is consistent with zero). CX42 appears to be a field star; its parallax distance is $2.2^{+0.3}_{-0.2} \text{ kpc}$, but its proper motion is completely inconsistent with M4. We note that CXs 30, 33, 63, 70, 97, 105, and 124 also have HST magnitudes (see column 5 in Table 10).

CX33 lies on the red giant branch of the *Gaia* CMD, consistent with its *HST* identification as an RS CVn type AB (Sec. 5.2). CX90 and CX105 have interestingly red colours for M4 members.

5.7 *VLA-Chandra* matches

We match the Shishkovsky et al. (2020, S20) VLA catalogue to the Bahramian et al. (2020, B20) *Chandra* catalogue to find positional matches (Table 11). We only consider sources that have confident or marginal detections in B20 (detection_quality_flag=0 or 1), excluding poor detections. To determine search radii, we first calculate source-specific composite positional errors ($\sigma_{r,x}$; r, x stands for ‘radio-X-ray’) by combining *Chandra* and VLA positional uncertainties in quadrature; this includes *Chandra* positional uncertainty characterised by the 95 per cent error radius (Hong et al. 2005), *Chandra* boresight offsets, and VLA positional error. The VLA positional errors in RA and Dec are set to the larger of the positional uncertainties reported in S20, and 0.1 of the projected beam sizes; the VLA error radius (denoted by σ_{VLA}) is set to the maximum of VLA positional errors in RA and Dec, of which the median is $\approx 0.10''$ for sources in M4. With search radii of $2.0\sigma_{r,x}$, we found 6 *Chandra* counterparts to VLA sources, one of which is a known MSP (CX12 = VLA9). Considering the low spatial densities of *Chandra* and VLA sources, it is very unlikely that these matches are coincidental (all are within $1.0 \sigma_{r,x}$).

What are radio sources likely to be? We summarize possibilities. For the radio spectral index α , ‘steeper’ sources have more negative α values, $\alpha = 0$ corresponds to a ‘flat’ source, and $\alpha > 0$ is termed ‘inverted.’ MSPs generally have very ‘steep’ radio spectra ($\alpha = -1.6 \pm 0.2$, Kramer et al. 1998), while background AGN and starbursts typically have moderately steep spectra ($\alpha = -0.7$, Gordon et al. 2021), and X-ray binaries typically have ‘flat’ spectra ($\alpha \sim 0$, Espinasse & Fender 2018). Only two MSPs with X-ray studies have $L_X < 3 \times 10^{29} \text{ erg s}^{-1}$ (Pichardo Marcano et al. 2023), our X-ray limit, indicating that MSPs should be X-ray detected in M4. Redback MSPs (with main-sequence companions) are X-ray brighter, $L_X > 7 \times 10^{30} \text{ erg s}^{-1}$ (e.g. Zhao & Heinke 2022). Coronal activity in close binaries can produce radio emission, following $L_X/L_R = 10^{15 \pm 1}$ (Güdel & Benz 1993), with typically flat spectra (Güdel 2002). This is potentially detectable for X-ray active binaries in M4, given the deep VLA radio limits of $10 \mu\text{Jy}$, which would imply $L_X = 4 \times 10^{31 \pm 1}$ following the Güdel-Benz relation. Güdel (2002) refer to BY Dra stars up to $10^{15} \text{ erg s}^{-1} \text{ Hz}^{-1}$ ($0.2 \mu\text{Jy}$ at M4), and RS CVn stars (coronally active binaries including giants) up to $10^{18} \text{ erg s}^{-1} \text{ Hz}^{-1}$ ($200 \mu\text{Jy}$ at M4), so evolved stars with coronal $L_X \sim 10^{31} \text{ erg s}^{-1}$ may plausibly be radio detected in M4.

5.8 VLA-HUGS matches

We also search VLA error circles for positional matches with HUGS sources. Since HUGS astrometry is matched to *Gaia* (within a few mas), we only use the VLA positional uncertainty. We use search radii of 3 times the VLA positional uncertainties (Section 5.7) and found a total of 7 matches including the known MSP (VLA9 or CX12); three of the matches have separations more than $2\sigma_{\text{VLA}}$. These matches are summarised in Table 12.

A more complete VLA-HUGS cross-match using the full VLA catalogue estimates ≈ 0.6 chance coincidences with MS sources per VLA source per arcsec^2 (Zhao, Y. et al., in prep); if a HUGS source marginally matches a VLA source, i.e., it has an offset of $3\sigma_{\text{VLA}} \approx 0.3''$, the false alarm rate is around 0.2.

5.9 Individual matches with VLA sources

We assume a core radius of 1.16 arcmin (Harris 1996, 2010 online version), and a distance of 1.85 kpc (Baumgardt et al. 2021).

VLA1/CX70 is the brightest among the 37 VLA sources in M4; its radio spectral index has an intermediate steepness ($\alpha = -0.71 \pm 0.01$). Its position coincides with CX70, the X-ray spectrum of which can be modelled by a power-law with a (relatively hard) photon index of $1.2^{+1.6}_{-1.1}$ (B20). We found no HUGS counterparts within the search region, but there is a faint red object barely visible in *V* and *I* (the area is not covered by the WFC3 UV filters). VLA1's radio and X-ray properties allow for the possibility of it being an MSP, though the optical non-detection would imply a very low-mass companion, likely a black widow system. However, these features could also be explained by a background AGN. Indeed, VLA1's radial offset ($2.2'$) from the cluster centre is about two core radii; using the normalised radio source counts in S20, we estimate ≈ 10 AGN with $S_5 > 10 \mu\text{Jy}$ within a radius of $2.2'$, so an AGN is likely.

VLA4 has a HUGS counterpart (R0009986) with a slight $UV_{275}-U_{336}$ excess in the ($UV_{275}, UV_{275}-U_{336}$) CMD, but is consistent with the MS in the other broad-band CMDs. In the colour-colour diagram (Fig. 5) the counterpart shows a significant $H\alpha$ deficit. R0009986 is a cluster member (PM member probability = 96.9 per cent). The optical position is only $0.04''$ from the VLA position, translating to 0.003 chance coincidences within a search circle at a radius of this offset. The radio spectrum is marginally steep enough to be consistent with a typical MSP ($\alpha = -0.4 \pm 0.1$), though MSPs, and especially reback MSPs (given the main sequence star identification), should be detected in X-rays (see above). Other interpretations also seem unlikely—an AGN is inconsistent with the high-confidence optical counterpart, an X-ray binary should show $H\alpha$ emission and $L_X \gtrsim 10^{30} \text{ erg s}^{-1}$, while the (relatively) bright radio emission, with strong limits on X-rays, makes a coronally active binary very unlikely. This leaves the nature of this system unclear.

VLA5 is positionally consistent (with a chance coincidence number of 0.2) with HUGS R0004648, which is a cluster member on the main sequence. The projected radial offset from the cluster centre is less than 1 arcmin, within which we expect ≈ 1 AGN. The steep radio spectrum ($\alpha = -1.4 \pm 0.1$) may suggest an MSP identification, though some AGN have such steep radio spectra. The MS photometry, $V_{606} = 19.8$ and $V_{606}-I_{814} = 1.3$, correspond to a K3-K4 dwarf of $0.3 M_{\odot}$, suggesting a reback MSP; however, the X-ray non-detection pushes the X-ray luminosity to $< 3 \times 10^{29} \text{ erg s}^{-1}$ —again, unusually low for a reback MSP. An AGN appears the most likely scenario, in which case the HUGS counterpart would be spurious.

VLA9/CX12 is the known MSP (Lyne et al. 1988; McKenna & Lyne 1988) PSR B1620–26 (or PSR M4 A, hereafter M4A). It is detected in the X-rays (CX12) and radio (M4-VLA9), with a quite steep radio spectrum ($\alpha < -2.60$). Its X-ray emission is consistent with thermal, blackbody-like radiation (see § A), as seen in most MSPs in other clusters (Bogdanov et al. 2006).

VLA13/CX77 is another steep-spectrum source ($\alpha = -1.2 \pm 0.6$) located at a relatively large projected distance (2.4 arcmin) from the cluster centre, which makes it more likely to be a background AGN. The absence of HUGS counterparts, if an MSP, would suggest a highly-ablated low-mass companion (a black widow), though an AGN is more likely.

VLA19/CX14 has an upper limit on α (< 1.3). The *Chandra* ID CX14 is within $1\sigma_{r,x}$, so the match is relatively confident. B20 found that a power-law model fits the X-ray spectrum best, giving a photon index of $2.5^{+1.0}_{-1.2}$ and L_X (0.5–10 keV) = $2.7^{+8.5}_{-1.5} \times 10^{30} \text{ erg s}^{-1}$. VLA19's large projected distance from the cluster centre (3.1 arcmin) indicates it is a background AGN.

VLA20 has a poorly determined radio spectral index ($\alpha < -0.4$). A HUGS ID (R0005914) consistent with the WD sequence is found at $2.1\sigma_{\text{VLA}}$ from the radio position. Despite this relatively large offset, this match is very unlikely to be a chance coincidence, due to the paltry number of WDs compared to MS stars. While R0005914 does not have a HUGS membership probability, its proximity to the cluster centre ≈ 1 arcmin argues against a background nature. The lack of X-rays argues against an MSP nature, but as the likely companion star is a white dwarf (rather than a main-sequence star, which would require a reback nature), this is more plausible than for VLA4 or VLA5 above.

VLA30/CX57 is a 5σ detection in both the low and high-frequency sub-bands, producing a spectral index of $\alpha = -0.2 \pm 0.8$. Its *Chandra* ID, CX57, is $0.6\sigma_{r,x}$ away from the radio position, so the match is relatively confident. CX57's X-ray spectrum can be fit by a power-law with a best-fit photon index of $1.0^{+1.7}_{-1.0}$. Similar to VLA1 and VLA13, a black widow scenario is possible, where the optical companion is very low-mass and faint. A distant AGN also fits the data, and seems most likely.

VLA31/CX8 is a flat-to-inverted ($\alpha = 0.4^{+0.6}_{-0.8}$) radio source that has both a HUGS (R0001877) and a *Chandra* ID (CX8). R0001877 is at a relatively large offset ($2.9\sigma_{\text{VLA}}$) from the radio position; however, it is a confident cluster member (PM = 97.5 per cent) that belongs to a rare population with unusual photometry—in all HUGS CMDs, it is located below the sub-giant branch and redder than the main sequence. In the ($H\alpha - R_{625}, V_{606} - I_{814}$) colour-colour diagram, R0001877 shows strong signs of $H\alpha$ emission. Objects in this region of CMDs are referred to as 'sub-subgiants' (SSGs; Leiner et al. 2022). SSGs in GCs are typically binary stars and X-ray sources, suggesting an evolutionary path distinct from that for single stars (Geller et al. 2017). So far, there are three cases of SSG-radio associations in GCs: two MSPs, PSR J1740-5340A and B, in NGC 6397 (Zhao et al. 2020; Zhang et al. 2022) match with steep radio sources, and an SSG matches a flat-to-inverted source in M10 (M10-VLA1) (Shishkovsky et al. 2018) that is likely a BH binary or an unusual RS CVn-type AB. The *Chandra* ID can be best modelled by a power-law, with a photon index of 2.5 ± 0.4 , consistent with typical accreting stellar-mass BHs in quiescence (e.g., Reynolds et al. 2014). VLA31's X-ray and radio luminosities make VLA31 consistent with the black hole $L_X - L_R$ correlation (Figure 9). The flat spectrum argues against an MSP nature, but does not completely rule it out. The radio and X-ray fluxes are consistent with the Güdel-Benz relation, within the (order of magnitude)

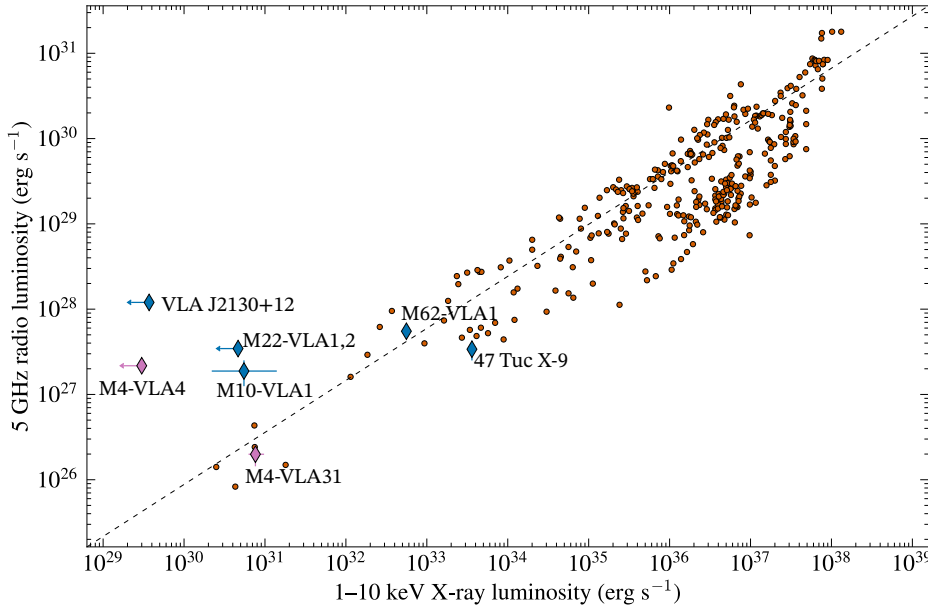
scatter, and the sub-subgiant star appears large enough to sustain substantial coronal activity, so this object may be an RS CVn.

Table 11. Six VLA counterparts to *Chandra* sources

M4-VLA	CX	Offset		S_5 (μJy)	S_7 (μJy)	α ($S_\nu \propto \nu^\alpha$)	Notes
		($''$)	($\sigma_{r,x}$)				
1	70	0.6	0.7	1289.40 ± 2.90	995.50 ± 3.50	$-0.71^{+0.01}_{-0.01}$	no PM info
9	12	0.2	0.3	40.50 ± 2.40	< 6.50	< -2.60	Known MSP
13	77	0.4	0.2	26.10 ± 2.80	16.90 ± 2.90	$-1.24^{+0.55}_{-0.61}$	no PM info
19	14	0.3	0.6	19.10 ± 3.70	< 14.70	< 1.30	no PM info
30	57	0.4	0.6	11.10 ± 2.10	10.60 ± 2.20	$-0.20^{+0.75}_{-0.82}$	no PM info
31	8	0.4	0.8	9.70 ± 2.70	12.20 ± 2.20	$0.37^{+0.59}_{-0.77}$	PM member

Table 12. UV/Optical counterparts to VLA sources.

M4-VLA	HUGS #	Offset		S_5 (μJy)	S_7 (μJy)	α ($S_\nu \propto \nu^\alpha$)	PM (%)	Notes
		($''$)	(σ_{VLA})					
4	R0009986	0.04	0.36	106.20 ± 2.50	90.50 ± 2.50	$-0.44^{+0.10}_{-0.10}$	96.9	slight UV excess
5	R0004648	0.25	2.42	82.70 ± 2.20	49.20 ± 2.10	$-1.43^{+0.10}_{-0.14}$	92.3	
9	R0006434	0.02	0.23	40.50 ± 2.40	< 6.50	< -2.60	–	Known MSP
20	R0005914	0.22	2.10	18.80 ± 2.60	< 7.30	< -0.40	96.4	WD
31	R0001877	0.30	2.89	9.70 ± 2.70	12.20 ± 2.20	$0.37^{+0.59}_{-0.77}$	97.5	H α excess; SSG


Figure 9. 5 GHz radio and 1–10 keV X-ray luminosity of quiescent/hard-state BHs (filled orange circles) and BH candidates found in GCs (filled blue diamonds) from the database compiled by [Bahramian & Rushton \(2022\)](#). The two radio sources in M4 which could possibly be black hole X-ray binaries, M4-VLA4 and M4-VLA31, are in pink, both of which are consistent with or above the quiescent/hard-state BH correlation (dashed line; [Gallo et al. 2014](#)).

6 MSP POPULATION IN M4

M4A (CX12/VLA9) is the only confirmed MSP in M4 (Sec. 5.9). [Kaluzny et al. \(2012\)](#) provided strong evidence that CX1 is likely to be a MSP, and likely a redback, as well. Using the correlation between stellar encounter rate and the number of MSPs in a GC, [Zhao & Heinke \(2022\)](#) predicted ~ 10 MSPs in M4, suggesting a few MSPs may remain undiscovered. In this section, we attempt to constrain the number of MSPs that might be hidden among the uncategorized X-ray sources.

Using the X-ray luminosities and fluxes in the 0.5–2 and 2–8 keV ranges from [Bahramian et al. \(2020\)](#), and optical identifications in Table 7, we plotted the X-ray CMD of M4 (Figure 10), comparing X-ray hardness with X-ray luminosity. Note that the X-ray flux ratios are calculated from the fitted power-law models in [Bahramian et al. \(2020\)](#), which gives a flux ratio limit at the assumed

parameter boundaries. Most of the sources of unknown nature are outside the core region, with distances to the centre > 1.5 arcmin, which *HST* observations do not cover. These objects are likely to be dominated by background AGN, and indeed we find that most have relatively hard X-ray colours, typical of background AGN (which often have substantial intrinsic absorption). We plotted the positions of 25 known cluster MSPs with $7 \times 10^{29} < L_X < 4 \times 10^{32} \text{ erg s}^{-1}$ (18 in 47 Tuc ([Heinke et al. 2005](#); [Bhattacharya et al. 2017](#)), 2 in ω Cen ([Zhao & Heinke 2022](#)), 2 in NGC 6397 ([Bogdanov et al. 2010](#)), 2 in Terzan 5 ([Bogdanov et al. 2021](#)), and one in M92 ([Zhao & Heinke 2022](#))), on the same X-ray CMD (navy-blue plus signs in Figure 10). We used the spectral fits in the listed sources, and their luminosities, to plot their positions, as the spectral response of *Chandra* changes with time. By comparing the colours and luminosities of those known MSPs with the positions of unknown

sources in M4, we identify a region in the X-ray CMD (shaded area in Figure 10) where unidentified MSPs are likely. While most MSPs' X-ray emission is dominated by thermal radiation from the surface, redback MSPs are dominated by harder shock emission, so we include a significant redback MSP sample from several clusters. These produce two overlapping loci on the X-ray CMD.

Within this region are 45 X-ray sources in M4, including 15 confident ABs (including 2 eclipsing AB candidates, CX25 and CX28), 2 likely ABs, 1 sub-subgiant/red giant, 1 blue straggler, 2 confident and 1 likely CV, 1 certain MSP (M4A/VLA9) and one good candidate (CX1), 1 likely foreground source (with a *Gaia* counterpart), and three unknown sources with *Gaia* counterparts. These objects we consider to have relatively confident identifications that are unlikely to be additional MSPs. We also note three objects discussed in § 5.9 which could possibly be candidate MSPs; CX8/VLA31 (a sub-subgiant), CX77/VLA13 and CX57/VLA30 (no HUGS counterparts). We also see another 16 unknown sources without *Gaia* counterparts. However, only three (CXs 17, 19, and 62) of those 16 unknown sources are covered by HST observations, showing empty error circles. As MSPs in a GC tend to be concentrated in the core, the 12 unknown sources located at distances >2 core radii (2.2 arcmin) from the centre, without additional information, are unlikely to be MSPs. We thus identify seven objects without optical counterparts, or with uncertain optical counterparts, in Table 13, which we consider as possible candidate MSPs. We estimate that $\lesssim 10$ MSPs remain undetected in M4, consistent with the estimate made from the correlation between stellar encounter rates and numbers of MSPs in GCs (Zhao & Heinke 2022).

Table 13. Candidate MSPs in M4

Source ^a	RA, Dec (J2000) ^b	L_X ^c (erg s^{-1})	Xcolour ^d	Dist ^e (arcmin)	Identification ^f from optical	VLA ID ^g
1	16:23:34.125–26:31:34.90	1.54E+32	−1.68	0.25	MSP?/qLMXB?	-
8	16:23:31.478–26:30:57.91	7.62E+30	0.85	1.02	SSG/??	31
17	16:23:35.984–26:31:01.71	2.24E+30	0.68	0.54	empty error	-
19	16:23:28.923–26:29:50.95	2.48E+30	0.90	2.20	empty error	-
57	16:23:30.245–26:30:45.12	2.79E+30	0.41	1.36	empty error	30
62	16:23:30.055–26:32:05.40	2.11E+30	1.96	1.23	empty error	-
77	16:23:41.592–26:29:37.81	1.16E+30	1.54	2.39	outside HUGS	13

Notes: ^aSource numbering in this work (Table 7). ^bSource position (Bahramian et al. 2020). ^cX-ray luminosity in erg s^{-1} , based on a BXA power-law fit (Bahramian et al. 2020). ^dX-ray colours from source fluxes in 0.5–2 keV and 2–8 keV. ^eSource distance from cluster centre in arcmin (Bahramian et al. 2020). ^fOptical identifications by *HST* observations (Table 7). ^gVLA counterparts to the X-ray sources listed (Table 11).

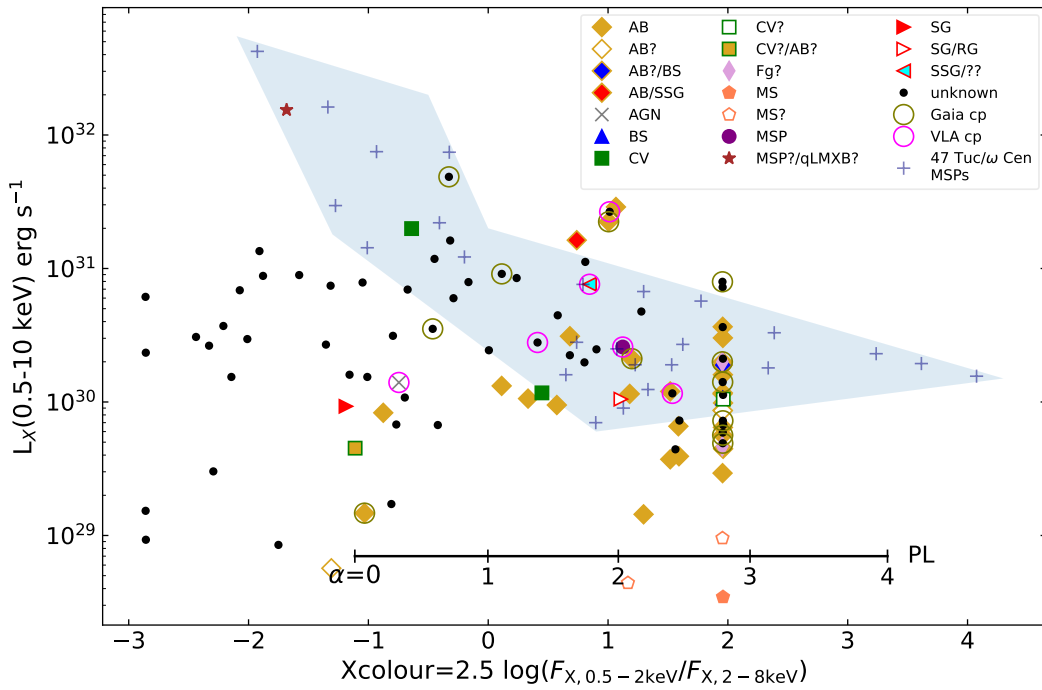


Figure 10. X-ray colour-magnitude diagram of M4, plotting X-ray luminosities in the band 0.5–10 keV vs. X-ray colours from source fluxes in 0.5–2 keV and 2–8 keV (Bahramian et al. 2020). Optical identifications from Table 7. We circle 12 sources with *Gaia* counterparts (olive circles; see Table 10), and six sources with VLA counterparts (magenta circles; see Table 11). Navy pluses represent 25 MSPs from other clusters (see text), while the shaded area indicates the region where we find these MSPs in the X-ray CMD. The X-ray colours of power-law models of different indices are also indicated.

7 RADIAL DISTRIBUTIONS

The radial distribution of a population of objects in a cluster depends on the characteristic mass of the objects. Populations of interest include all *Chandra* sources, bright CVs, faint CVs, ABs, and blue stragglers. Analysis of population radial distributions to determine object masses relative to the main sequence turnoff (MSTO) mass have been performed for a number of clusters. These include 47 Tuc (Grindlay et al. 2002; Heinke et al. 2005; Cheng et al. 2019a), M30 (Lugger et al. 2007; Mansfield et al. 2022), M71 (Elsner et al. 2008), NGC 6397 (Cohn et al. 2010), NGC 6752 (Lugger et al. 2017; Cohn et al. 2021), Terzan 5 (Cheng et al. 2019b), M28 (Cheng et al. 2020a), and ω Cen (Cheng et al. 2020b). Estimated object masses provide an important information on their nature. For CV candidates in particular, binary system mass estimates provide a measure of the masses of the white dwarf primaries, which provides an important constraint on CV evolution (Pala et al. 2022).

The method of characteristic mass determination in these studies is based on the assumption that the populations with members more massive than the main-sequence turnoff (MSTO) mass are in thermal equilibrium. In this case, the greater the characteristic mass of a population, the higher its degree of central concentration. Our analysis algorithm has most recently been described by Cohn et al. (2021). The essential component is a maximum-likelihood fitting of a generalised King model to the radial distribution of each population, including a MSTO group. The surface density profile of the generalised King model takes the form,

$$S(r) = S_0 \left[1 + \left(\frac{r}{r_0} \right)^2 \right]^{\alpha/2}. \quad (1)$$

The core radius r_c , defined as the radius where the surface density drops to half of its central value, is related to the scale parameter r_0

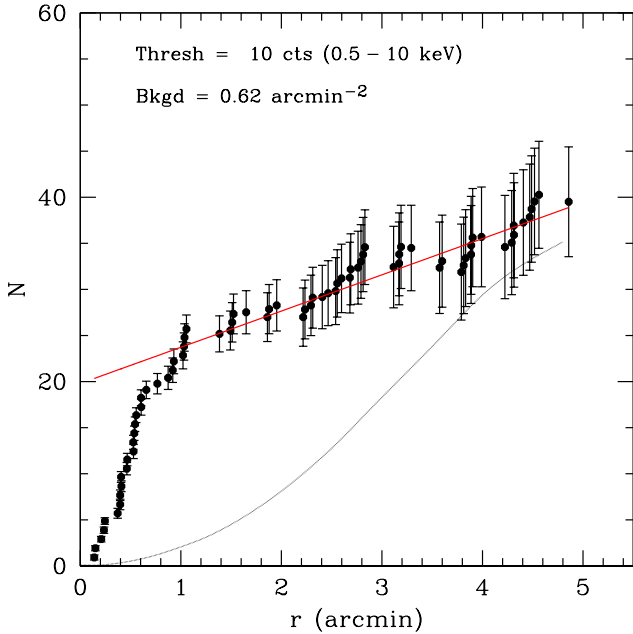


Figure 11. Cumulative radial distribution of excess Chandra source counts over the background predicted from the [Giacconi et al. \(2001\)](#) extragalactic source counts. Error bars represent the statistical uncertainty of the background correction. The dashed curve is the cumulative background distribution for the expected background density of 0.62 arcmin^{-2} .

by,

$$r_c = \left(2^{-2/\alpha} - 1\right)^{1/2} r_0. \quad (2)$$

For the MSTO sample, $\alpha \approx -2$ and $r_c \approx r_0$. These parameter values may either be determined from a fit of Eqn. 1 to the MSTO sample or by the adoption of a King-model profile and the determination of the optical core radius. While we attempted to determine both α and r_c for the MSTO sample directly from the HUGS V_{606} -band star counts, this approach is complicated by the large core of M4, which fills much of the *HST* ACS/WFC field. We also explored adopting a value of $\alpha = -2$ and determining r_c , which results in a value of $r_c = 65.4 \pm 3.3 \text{ arcsec}$. Two studies have determined the core radius of M4 by fitting King models to the ground-based surface brightness profile presented by [Trager et al. \(1995\)](#), producing different results. These are 50.1 arcsec ([Trager et al. 1995](#)) and 69.7 arcsec ([McLaughlin & van der Marel 2005](#)). Additionally, [Baumgardt et al. \(2021\)](#) obtained a value of 43.5 arcsec by fitting an N-body model to a set of ground and space-based data. We conclude that the determination of r_c for M4 is somewhat uncertain.

A refinement of our determination of the characteristic *Chandra* source mass in the present study is that we now incorporate an X-ray exposure map, which allows us to select those pixels in the *Chandra* image that satisfy a minimum exposure criterion. This allows the removal from consideration of those regions that received either no or inadequate exposure. A second refinement concerns the application of the background source correction for the *Chandra* source sample. We now generate 1000 bootstrap resamplings of the original source sample and for each of these we generate 1000 Monte-Carlo removals of N_{bkgd} uniformly distributed objects, where N_{bkgd} is chosen as a random Poisson deviate with an expectation value equal to the predicted extragalactic source number calculated from [Giacconi et al. \(2001\)](#).

This procedure results in a determination of the value of the mass ratio $q_X = m_X/m_{\text{MSTO}}$. We note that in our recent analyses of the entire *Chandra* source distributions for NGC 6752 in [Lugger et al. \(2017\)](#) and [Cohn et al. \(2021\)](#), we neglected to apply a background correction. This resulted in a moderate underestimate of the mass of the typical *Chandra* source in these studies. For comparison, [Cohn et al. \(2021\)](#) obtained a value of $q_X = 1.25 \pm 0.10$ for NGC 6752, while [Heinke et al. \(2005\)](#) obtained $q_X = 1.63 \pm 0.11$ for 47 Tuc; these values differ at the 2.6σ level.

Fig. 11 shows the cumulative excess number of sources (for a 10-count detection threshold) over the expected background number, calculated for a background density of 0.62 arcmin^{-2} , based on [Giacconi et al. \(2001\)](#). The red dashed line shows a linear regression fit to this profile for $r > 3 \text{ arcmin}$. The expectation is that the profile should be asymptotically flat at large r , as the incremental contribution of the cluster to the total source counts dwindles. The continuous rise of the red line suggests the presence of an excess number of about 11 cluster sources in the halo, between 2 and 5 arcmin from the cluster centre. Such an extended-halo X-ray source population has been observed in 47 Tuc by [Cheng et al. \(2019a\)](#), who interpret it as having descended from a primordial binary population in the cluster halo.

For the adopted background density of 0.62 arcmin^{-2} and a core radius value of 50.1 arcsec ([Trager et al. 1995](#)), the maximum-likelihood fit to a limiting radius of 5 arcmin of a generalised King model produces a mass ratio value of $q_X = 1.53^{+0.25}_{-0.22}$. The greater uncertainty limits relative to 47 Tuc are likely due to the larger background correction for M4 as a result of its greater proximity and thus larger angular size on the sky. For the 74 10-count sources within 5 arcmin of the cluster centre that meet the minimum exposure criterion, 35 are likely background objects. For the same background density of 0.62 arcmin^{-2} and a core radius of 69.7 arcsec ([McLaughlin & van der Marel 2005](#)), $q_X = 1.84^{+0.38}_{-0.31}$. These two values for q_X are consistent to within the large uncertainty range. The corresponding range in typical source mass is $m_x \sim 1.2 - 1.5 M_\odot$.

We next determine the q value for the AB group. In this case, no background correction is necessary, since all of the AB candidates are likely cluster members, as indicated by their proper motions. The result depends somewhat sensitively on the value adopted for the core radius. For $r_c = 50.1 \text{ arcsec}$, $q_{\text{AB}} = 1.79^{+0.32}_{-0.27}$, while for $r_c = 69.7 \text{ arcsec}$, $q_{\text{AB}} = 2.49^{+0.49}_{-0.43}$. Although these two values are formally consistent with each other, given the large uncertainty, the q_{AB} value for the smaller core radius is much more similar to the range of q_X values for all of the X-ray sources. Since the ABs are by far the largest subgroup of X-ray sources, this suggests that the smaller core radius value is the more appropriate one for this analysis. For a MSTO mass of $0.80 M_\odot$ and a core radius of 50.1 arcsec , the inferred characteristic mass of the ABs is $1.43^{+0.26}_{-0.22} M_\odot$. For comparison, [Cohn et al. \(2010\)](#) obtained a smaller characteristic mass of $1.06 \pm 0.08 M_\odot$ for a sample of 36 ABs in NGC 6397. These two values do not differ significantly, given the large uncertainty of the M4 AB characteristic mass estimate.

8 CONCLUSIONS

Previous *Chandra* and *HST* data of M4 revealed 20 optical counterparts to 31 X-ray sources ([Bassa et al. 2004, 2005](#); [Kaluzny et al. 2012](#)). Here we have used an X-ray source list ([Bahramian et al. 2020](#)) from significantly deeper *Chandra* observations (119 ks, vs. 26 ks used by [Bassa et al. 2004](#)), and analyzed *HST* broad-band

optical and ultraviolet data using the ACS and WFC3 filters, largely from the HUGS survey.⁶ We also discuss MAVERIC radio imaging data using the Jansky VLA, which finds 38 radio sources within M4 (Shishkovsky et al. 2020).

We consider 88 high-quality *Chandra* sources within the 4.3 arcmin half-light radius of M4, of which 53 are covered by some HST data, and 16 were previously identified. We add 24 new HST optical/UV confident counterparts. In total, we find 28 confident ABs, and 6 other likely coronal sources (2 AB candidates, 1 blue straggler, 2 subgiants, 1 red giant), for 34 likely coronally-emitting sources in the HST/ACS field. We also find two confident CVs (CX4 and CX76, which is new) and two CV candidates (CX81 and CX101), along with a known MSP (CX12) and a previously suggested candidate MSP (CX1). We find one new foreground source (CX63), and 8 empty error circles, likely dominated by distant AGN (as ~ 7 background AGN are expected in this region, and 1 empty error circle also shows a radio source). Using *Gaia* data, we identify seven brighter likely optical counterparts outside the HST coverage.

We also identify 9 potential matches between VLA radio sources and X-ray or optical sources (6 X-ray, 5 optical). Some are almost certainly AGN (e.g. VLA1/CX70), but some appear highly likely to be cluster sources (VLA9/CX12 is a known MSP; VLA31/CX8, a sub-subgiant, and VLA20, a WD, appear to be cluster members). Our knowledge of the nature of faint cluster radio sources is quite limited so far.

We attempt to identify potential candidate MSPs in M4 without detected radio pulsations so far. Among X-ray sources, we agree with Kaluzny et al. (2012) that CX1 is a likely MSP (probably a redback); its lack of detected radio emission may be due to radio eclipses, faintness, or a misaligned beam geometry. CX8/VLA31 has a sub-subgiant optical counterpart. While its X-ray properties are consistent with MSPs, its flat radio spectrum would be unusual; dedicated spectroscopy of this object will be reported elsewhere. We identify another five objects with X-ray properties similar to MSPs but without optical counterparts, two of which have radio counterparts. A few other VLA-detected radio sources (VLA5 and VLA20) with possible optical counterparts have steep spectra, suggestive of MSPs, but their X-ray upper limits make an MSP nature unlikely. Assuming that MSPs in M4 resemble those in other globular clusters, we conservatively constrain the number of MSPs in M4 to < 10 .

The background-corrected radial distribution of 10-count *Chandra* sources suggests a relaxed population of 27 sources within the central 2 arcmin, with average mass $\sim 1.2 - 1.5 M_{\odot}$, as well as a cluster halo population of ~ 10 sources. The majority of these cluster sources, within both the region covered by the HUGS field and the cluster halo, are likely to be ABs.

We can compare the numbers of different object types in M4 to other well-studied clusters, at similar L_X limits (Tables 1, 2). We now have two confirmed, plus two candidate CVs, in M4, down to $\log L_X = 29.5$; this agrees with the predicted number of four CVs produced per unit stellar mass in the field. NGC 6397, with a similar mass as M4, has almost four times as many CVs as M4 (this is also true for $L_X > 10^{30}$ erg s⁻¹, or for $L_X > 10^{31}$ erg s⁻¹), suggesting dynamical production of NGC 6397's CVs. Although the number

of CVs in M4 is small, their optical and X-ray luminosity functions seem to be consistent with those in other clusters (Cohn et al. 2010; Rivera Sandoval et al. 2018; Lugger et al. 2017; Belloni et al. 2019). Interestingly, which CVs are ‘bright’ or ‘faint’ differs depending on whether one is referring to X-rays or M_V ; CX4 has $L_X = 2 \times 10^{31}$ erg s⁻¹ but $M_V \sim 8$, while CX76 has $L_X = 1.2 \times 10^{30}$ erg s⁻¹ but $M_V \sim 6$.

MSP progenitors are dynamically produced in clusters (Clark 1975), and indeed the numbers of MSPs known⁷ in the nearby globular clusters NGC 6397 (2), NGC 6752 (9), 47 Tucanae (29), and M22 (4) are similar to their predicted stellar encounter rates compared to M4 (3, 15, 37, 3 respectively; Bahramian et al. 2013), although ω Cen has significantly more MSPs (18) than predicted (3, Chen et al. 2023).

Finally, M4 and NGC 6397 have similar numbers of ABs with $L_X > 3 \times 10^{29}$ erg s⁻¹ (a limit to which both clusters are fairly complete in identifications), 28 vs. 26. This is consistent with the similarity in their masses. However, it is somewhat surprising when compared to the dramatically different binary fractions in the two clusters (10 per cent at the half-mass radius for M4, 2.4 per cent for NGC 6397; Milone et al. 2012). We resolve this apparent contradiction by noting that X-ray detectable ABs are generally in much tighter orbits than average binaries in clusters (e.g. Heinke et al. 2005 detect X-rays from most short-period binaries found by Albrow et al. 2001 in 47 Tuc). Thus, this indicates that although the total binary fractions differ significantly, the short-orbit (or ‘hard’) binary fraction is similar between M4 and NGC 6397. This seems to be in agreement with simulations that indicate that hard binaries are not substantially destroyed by cluster dynamics (e.g. Hurley et al. 2007), but that the binary fraction differences may be explained by destruction of ‘soft’ (wide-orbit) binaries in denser clusters, perhaps especially during a higher-density initial cluster formation phase (Fregeau et al. 2009; Leigh et al. 2015).

We note promising future directions regarding this cluster. First, the radio sources associated with cluster members, apart from the known millisecond pulsar, are mysterious; optical spectroscopic studies are in progress. A second epoch of HST *B* data would permit proper motion membership to be ascertained for the faintest objects. In particular, the faintest CV candidate, CX101, has very limited photometry, with its apparent strong *H α* excess being very low signal-to-noise.

ACKNOWLEDGEMENTS

We thank the anonymous referee for thoughtful comments that improved the manuscript. We acknowledge useful discussions with M. van den Berg, D. Pooley, and J. Strader. M. Legnardi generously provided differential-reddening-corrected photometry for M4. CH acknowledges support from NSERC Discovery Grant RGPIN-2016-04602. JZ is supported by a China Scholarship Council scholarship No. 202108180023. This work is based on observations made with the NASA/ESA *Hubble Space Telescope* obtained from the Space Telescope Science Institute, which is operated by the Association of Universities for Research in Astronomy, Inc., under NASA contract NAS 5-26555. The results reported in this article are based in part on observations made by the *Chandra X-ray Observatory*. Funding for the *Gaia* Data Processing and Analysis Consortium has

⁶ A caveat is that our HST data (3.4×3.4 arcmin FoV) do not fully cover the 4.3 arcmin half-light radius, only 20 per cent of it. However, since the HST/ACS data cover 53 of the 88 high-quality *Chandra* detections within the half-light radius, and we anticipate ~ 30 background sources in the remaining area (see Section 7, and cf. Heinke et al. 2005), this is not a strong caveat.

⁷ <http://www.naic.edu/~pfreire/GCpsr.html>, as of January 2023

been provided by national institutions, in particular the institutions participating in the *Gaia* Multilateral Agreement.

DATA AVAILABILITY

The *Chandra* data used in this paper are available in the *Chandra* Data Archive (<https://cxc.harvard.edu/cda/>) by searching the Observation ID listed in Section A in the Search and Retrieval interface, ChaSeR (<https://cda.harvard.edu/chaser/>). The *HST* data used in this work can be retrieved from the Mikulski Archive for Space Telescope (MAST) Portal (<https://mast.stsci.edu/search/ui/#/hst>) by searching the proposal IDs listed in Table 3. The VLA observations are available at <https://data.nrao.edu/portal/#/> under the proposal IDs VLA/13B-014 and VLA/15A-100. This work has made use of data from the European Space Agency (ESA) mission *Gaia* (<https://www.cosmos.esa.int/gaia>), processed by the *Gaia* Data Processing and Analysis Consortium (DPAC, <https://www.cosmos.esa.int/web/gaia/dpac/consortium>).

REFERENCES

- Albrow M. D., et al., 2001, *ApJ*, 559, 1060
- Anderson J., et al., 2008, *AJ*, 135, 2055
- Bagchi M., Lorimer D. R., 2011, in Burgay M., et al., eds, American Institute of Physics Conference Series Vol. 1357, Radio Pulsars: An Astrophysical Key to Unlock the Secrets of the Universe. pp 173–176 ([arXiv:1012.4705](https://arxiv.org/abs/1012.4705)), doi:10.1063/1.3615109
- Bahramian A., Rushton A., 2022, *bersavosh/HRB-LrLx_pub*: update 220808, Zenodo, doi:10.5281/zenodo.6972578
- Bahramian A., Heinke C. O., Sivakoff G. R., Gladstone J. C., 2013, *ApJ*, 766, 136
- Bahramian A., et al., 2015, *MNRAS*, 452, 3475
- Bahramian A., et al., 2020, *ApJ*, 901, 57
- Bailer-Jones C. A. L., et al., 2021, *AJ*, 161, 147
- Bassa C., et al., 2004, *ApJ*, 609, 755
- Bassa C., et al., 2005, *ApJ*, 619, 1189
- Baumgardt H., et al., 2021, Fundamental parameters of Galactic globular clusters (as of May 2021), <https://people.smp.uq.edu.au/HolgerBaumgardt/globular/>
- Beaumont C., Goodman A., Greenfield P., 2015, in Taylor A. R., Rosolowsky E., eds, Astronomical Society of the Pacific Conference Series Vol. 495, Astronomical Data Analysis Software and Systems XXIV (ADASS XXIV). p. 101
- Beccari G., De Marchi G., Panagia N., Pasquini L., 2014, *MNRAS*, 437, 2621
- Belloni D., et al., 2019, *MNRAS*, 483, 315
- Bhattacharya S., et al., 2017, *MNRAS*, 472, 3706
- Bogdanov S., et al., 2006, *ApJ*, 646, 1104
- Bogdanov S., et al., 2010, *ApJ*, 709, 241
- Bogdanov S., et al., 2021, *ApJ*, 912, 124
- Chabrier G., 2001, *ApJ*, 554, 1274
- Chen W., et al., 2023, *MNRAS*,
- Cheng Z., Li Z., Xu X., Li X., 2018, *ApJ*, 858, 33
- Cheng Z., et al., 2019a, *ApJ*, 876, 59
- Cheng Z., et al., 2019b, *ApJ*, 883, 90
- Cheng Z., et al., 2020a, *ApJ*, 892, 16
- Cheng Z., et al., 2020b, *ApJ*, 904, 198
- Clark G. W., 1975, *ApJ*, 199, L143
- Cohn H. N., et al., 2010, *ApJ*, 722, 20
- Cohn H. N., et al., 2021, *MNRAS*, 508, 2823
- Cool A. M., et al., 1995, *ApJ*, 439, 695
- Cool A. M., et al., 2013, *ApJ*, 763, 126
- Davies M. B., 1997, *MNRAS*, 288, 117
- De Marchi G., Panagia N., Romaniello M., 2010, *ApJ*, 715, 1
- Dotter A., et al., 2007, *AJ*, 134, 376
- Edmonds P. D., Gilliland R. L., Heinke C. O., Grindlay J. E., 2003a, *ApJ*, 596, 1197
- Edmonds P. D., Gilliland R. L., Heinke C. O., Grindlay J. E., 2003b, *ApJ*, 596, 1177
- Elsner R. F., et al., 2008, *ApJ*, 687, 1019
- Espinasse M., Fender R., 2018, *MNRAS*, 473, 4122
- Fregeau J. M., Ivanova N., Rasio F. A., 2009, *ApJ*, 707, 1533
- Fruscione A., et al., 2006, in Silva D. R., Doxsey R. E., eds, Society of Photo-Optical Instrumentation Engineers (SPIE) Conference Series Vol. 6270, Society of Photo-Optical Instrumentation Engineers (SPIE) Conference Series. p. 62701V, doi:10.1117/12.671760
- Gaia Collaboration et al., 2016, *A&A*, 595, A1
- Gaia Collaboration et al., 2022, arXiv e-prints, p. arXiv:2208.00211
- Gallo E., et al., 2014, *MNRAS*, 445, 290
- Ge C., et al., 2015, *ApJ*, 812, 130
- Gehrels N., 1986, *ApJ*, 303, 336
- Geller A. M., et al., 2017, *ApJ*, 840, 66
- Giacconi R., et al., 2001, *ApJ*, 551, 624
- Gordon Y. A., et al., 2021, *ApJS*, 255, 30
- Grindlay J. E., Heinke C., Edmonds P. D., Murray S. S., 2001a, *Science*, 292, 2290
- Grindlay J. E., et al., 2001b, *ApJ*, 563, L53
- Grindlay J. E., et al., 2002, *ApJ*, 581, 470
- Güdel M., 2002, *ARA&A*, 40, 217
- Guedel M., Benz A. O., 1993, *ApJ*, 405, L63
- Haggard D., Cool A. M., Davies M. B., 2009, *ApJ*, 697, 224
- Hansen B. M. S., et al., 2004, *ApJS*, 155, 551
- Harding A. K., Muslimov A. G., 2002, *ApJ*, 568, 862
- Harris W. E., 1996, *AJ*, 112, 1487
- Heinke C. O., et al., 2003, *ApJ*, 598, 501
- Heinke C. O., et al., 2005, *ApJ*, 625, 796
- Heinke C. O., Rybicki G. B., Narayan R., Grindlay J. E., 2006, *ApJ*, 644, 1090
- Heinke C. O., et al., 2020, *MNRAS*, 492, 5684
- Hellier C., 2001, Cataclysmic Variable Stars: How and Why They Vary. Springer-Praxis
- Henleywillis S., et al., 2018, *MNRAS*, 479, 2834
- Hong J., et al., 2005, *ApJ*, 635, 907
- Howell S. B., Nelson L. A., Rappaport S., 2001, *ApJ*, 550, 897
- Hurley J. R., Aarseth S. J., Shara M. M., 2007, *ApJ*, 665, 707
- Hut P., et al., 1992, *PASP*, 104, 981
- Ivanova N., Belczynski K., Fregeau J. M., Rasio F. A., 2005, *MNRAS*, 358, 572
- Ivanova N., et al., 2006, *MNRAS*, 372, 1043
- Johnston H. M., Verbunt F., 1996, *A&A*, 312, 80
- Kaluzny J., Thompson I. B., Krzeminski W., 1997, *AJ*, 113, 2219
- Kaluzny J., et al., 2012, *ApJ*, 750, L3
- Kaluzny J., Thompson I. B., Rozycka M., Krzeminski W., 2013, *Acta Astron.*, 63, 181
- Knigge C., 2012, *Mem. Soc. Astron. Italiana*, 83, 549
- Knigge C., et al., 2003, *ApJ*, 599, 1320
- Kong A. K. H., et al., 2006, *ApJ*, 647, 1065
- Kramer M., et al., 1998, *ApJ*, 501, 270
- Kremer K., et al., 2020, in Bragaglia A., Davies M., Sills A., Vesperini E., eds, Vol. 351, Star Clusters: From the Milky Way to the Early Universe. pp 357–366 ([arXiv:1907.12564](https://arxiv.org/abs/1907.12564)), doi:10.1017/S1743921319007269
- Legnardi M. V., et al., 2023, *MNRAS*, 522, 367
- Leigh N. W. C., et al., 2015, *MNRAS*, 446, 226
- Leiner E. M., et al., 2022, *ApJ*, 927, 222
- Lugger P. M., et al., 2007, *ApJ*, 657, 286
- Lugger P. M., et al., 2017, *ApJ*, 841, 53
- Lyne A. G., et al., 1988, *Nature*, 332, 45
- Mansfield S., et al., 2022, *MNRAS*, 511, 3785
- McKenna J., Lyne A. G., 1988, *Nature*, 336, 226
- McLaughlin D. E., van der Marel R. P., 2005, *ApJS*, 161, 304
- Miller-Jones J. C. A., et al., 2015, *MNRAS*, 453, 3918

Milone A. P., et al., 2012, *A&A*, **540**, A16
 Mochejska B. J., Kaluzny J., Thompson L., Pych W., 2002, *AJ*, **124**, 1486
 Nardiello D., et al., 2018, *MNRAS*, **481**, 3382
 Nascimbeni V., et al., 2014, *MNRAS*, **442**, 2381
 Pala A. F., et al., 2020, *MNRAS*, **494**, 3799
 Pala A. F., et al., 2022, *MNRAS*, **510**, 6110
 Pallanca C., et al., 2017, *ApJ*, **845**, 4
 Pichardo Marcano M., et al., 2023, *MNRAS*, **521**, 5026
 Piotto G., et al., 2015, *AJ*, **149**, 91
 Pooley D., 2015, in IAU General Assembly. p. 2257028
 Pooley D., 2016, *Mem. Soc. Astron. Italiana*, **87**, 547
 Pooley D., Hut P., 2006, *ApJ*, **646**, L143
 Pooley D., et al., 2002, *ApJ*, **569**, 405
 Pooley D., et al., 2003, *ApJ*, **591**, L131
 Pretorius M. L., Knigge C., 2012, *MNRAS*, **419**, 1442
 Reynolds M. T., et al., 2014, *MNRAS*, **441**, 3656
 Ridolfi A., et al., 2021, arXiv e-prints, p. arXiv:2103.04800
 Rivera Sandoval L. E., et al., 2018, *MNRAS*, **475**, 4841
 Robitaille T., et al., 2017, glueviz v0.13.1: multidimensional data exploration, doi:10.5281/zenodo.1237692
 Rucinski S., 1995, *PASP*, **107**, 648
 Shara M. M., Hurley J. R., 2006, *ApJ*, **646**, 464
 Shishkovsky L., et al., 2018, *ApJ*, **855**, 55
 Shishkovsky L., et al., 2020, *ApJ*, **903**, 73
 Sigurdsson S., et al., 2003, *Science*, **301**, 193
 Stassun K. G., Torres G., 2021, *ApJ*, **907**, L33
 Taylor M. B., 2005, in Shopbell P., Britton M., Ebert R., eds, *Astronomical Society of the Pacific Conference Series Vol. 347, Astronomical Data Analysis Software and Systems XIV*. p. 29
 Taylor J. M., Grindlay J. E., Edmonds P. D., Cool A. M., 2001, *ApJ*, **553**, L169
 Thomson G. S., et al., 2012, *MNRAS*, **423**, 2901
 Thorsett S. E., Arzoumanian Z., Camilo F., Lyne A. G., 1999, *ApJ*, **523**, 763
 Trager S. C., King I. R., Djorgovski S., 1995, *AJ*, **109**, 218
 Vasiliev E., 2019, *MNRAS*, **484**, 2832
 Verbunt F., 2000, in Pallavicini R., Micela G., Sciortino S., eds, *Astronomical Society of the Pacific Conference Series Vol. 198, Stellar Clusters and Associations: Convection, Rotation, and Dynamics*. p. 421 (arXiv:astro-ph/9907202)
 Verbunt F., 2001, *A&A*, **368**, 137
 Verbunt F., 2002, in van Leeuwen F., Hughes J. D., Piotto G., eds, *Astronomical Society of the Pacific Conference Series Vol. 265, Omega Centauri, A Unique Window into Astrophysics*. p. 289 (arXiv:astro-ph/0111441), doi:10.48550/arXiv.astro-ph/0111441
 Verbunt F., Pooley D., Bassa C., 2008, in Vesperini E., Giersz M., Sills A., eds, *Proceedings of the International Astronomical Union Vol. 246, Dynamical Evolution of Dense Stellar Systems*. pp 301–310 (arXiv:0710.1804), doi:10.1017/S1743921308015822
 Vesperini E., 2010, *Philosophical Transactions of the Royal Society of London Series A*, **368**, 829
 Wilms J., Allen A., McCray R., 2000, *ApJ*, **542**, 914
 Zhang L., et al., 2022, *ApJ*, **934**, L21
 Zhao J., Heinke C. O., 2022, *MNRAS*, **511**, 5964
 Zhao Y., et al., 2020, *MNRAS*, **493**, 6033
 Zhao Y., et al., 2021, *ApJ*, **914**, 77
 van den Berg M., 2020, in Bragaglia A., Davies M., Sills A., Vesperini E., eds, *Vol. 351, Star Clusters: From the Milky Way to the Early Universe*. pp 367–376 (arXiv:1910.07595), doi:10.1017/S1743921319007981

APPENDIX A: X-RAY ANALYSIS OF THE MSP M4A

We used archived CXO ACIS-S X-ray observations of M4 (observation IDs 946, 7446, and 7447) to analyze the X-ray properties of M4A, with a total exposure time of 119.2 ks. We reduced and ex-

Table A1. Spectral fits for PSR B1620–26 in M4.

	Spectral Model		
	BB	NSA	PL
$kT_{\text{BB}}/\log T_{\text{eff}}/\Gamma^a$	0.30 ± 0.03	6.34 ± 0.08	2.8 ± 0.3
Reduced Stat.	1.06	0.99	1.36
Q-value	0.39	0.44	0.21
$F_X(0.5\text{--}6\text{ keV})^b$	$4.4^{+0.8}_{-1.0}$	$4.6^{+2.5}_{-1.3}$	$9.5^{+2.0}_{-2.0}$

Notes: N_{H} was fixed for all fits at $3.05 \times 10^{21} \text{ cm}^{-2}$.

^a kT_{BB} : blackbody temperature in units of keV; $\log T_{\text{eff}}$: unredshifted effective temperature of the NS surface in units of log Kelvin; Γ : photon index.

^b Unabsorbed flux in units of $10^{-15} \text{ erg cm}^{-2} \text{ s}^{-1}$.

tracted data using CIAO⁸ (Fruscione et al. 2006), version 4.13, CALDB 4.9.4. All the *Chandra* data were first reprocessed to generate new level 2 files for further analysis through the *chandra_repro* script. No background flares were found for those observations.

We searched for an X-ray counterpart to M4A using its radio timing position. We applied *wavdetect*, a Mexican-Hat Wavelet source detection script, to identify sources and generate regions for spectral extraction using *specextract*. The X-ray spectra of M4A were combined for spectral fitting using the *combine_spectra* script. The corresponding background spectra were extracted from source-free regions around M4A.

We performed X-ray spectral fitting in *SHERPA*, the modelling and fitting package of CIAO. We first filtered the energy range to 0.5–6 keV. (The full spectrum suggests hard-to-model flux above 6 keV; but a merged image of the region does not show evidence of a source above 6 keV. We chose to ignore data above 6 keV for this work.) Data were grouped to five counts per bin. We applied *wstat* statistics in *SHERPA* to estimate fitting uncertainties and goodness. The X-ray absorption by the interstellar medium towards M4 was modelled by *xstbabs* with *wilm* abundances (Wilms et al. 2000). The hydrogen column number density (N_{H}) was fixed to $3.05 \times 10^{21} \text{ cm}^{-2}$, which was obtained by converting the interstellar reddening to the cluster, $E(B-V) = 0.35$ (Harris 1996, 2010 edition), to N_{H} using the conversion of Bahramian et al. (2015).

We considered three spectral models to fit the X-ray emission from M4A: a blackbody (BB; *xsbbodyrad*), a neutron star hydrogen atmosphere model (NSA; *xsnstatmos*, see Heinke et al. 2006), and a power-law model (PL; *xspgpwr1w*). For the NSA model, we fixed the NS mass and radius parameters to $1.4 M_{\odot}$ and 10 km, respectively, and the distance to M4 was set to 1.85 kpc (Baumgardt et al. 2021). The fitting results are given in Table A1.

The X-ray spectrum of M4A in the band 0.5–6 keV is well described by a single BB or NSA model, consistent with thermal emission from this source. For a single PL model, the best-fit photon index is 2.8 ± 0.3 . Typically, nonthermal emission from MSPs (e.g. synchrotron) can be represented by a power-law of photon index 1–2, while thermal blackbody-like surface emission can be fit by a blackbody, or (for relatively low-count spectra) by a power-law of index $\gg 2$. The fit parameters for M4A suggest that its emission is largely thermal surface emission. We also tested spectral fitting with combinations of PL and BB/NSA models, but the additional component does not improve the fit. The spectral fitting results of M4A indicate that the X-ray emission is principally thermal and hence likely originates from hotspots near the magnetic poles on the NS surface, heated by returning particles from the magnetosphere (Harding & Muslimov 2002). The 0.5–6 keV X-ray

⁸ <https://cxc.cfa.harvard.edu/ciao/>

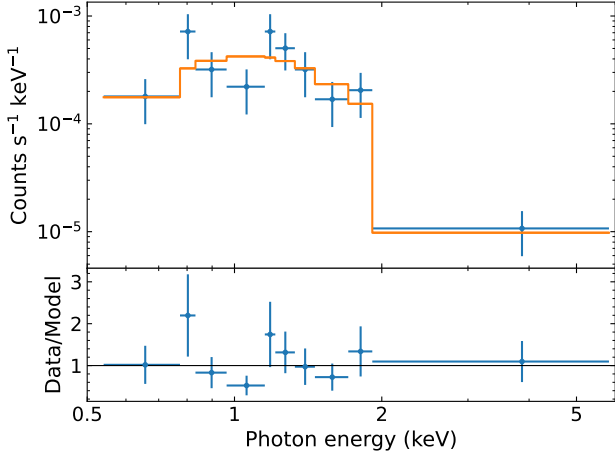


Figure A1. The X-ray spectrum and best fit of M4A. Data are filtered into the energy band of 0.5–6 keV and grouped to five counts per bin. The spectrum is well fitted by a single NSA model, using `wstat` statistics.

luminosity inferred from the NSA model is $L_X = 1.9^{+1.0}_{-0.5} \times 10^{30}$ erg s^{-1} , for a distance of 1.85 ± 0.02 kpc (Baumgardt et al. 2021). The X-ray spectrum and best-fit NSA model are shown in Figure A1.

APPENDIX B: FINDING CHARTS

(This material is intended for online distribution only.)

This paper has been typeset from a $\text{\TeX}/\text{\LaTeX}$ file prepared by the author.